NOAA Technical Memorandum OAR GSL-77
https://doi.org/10.25923/rahr-sj70

A Description of the MYNN-EDMF Turbulence Scheme

Joseph B. Olson, Wayne M. Angevine, David D. Turner, Xia Sun, Julia M. Simonson,
Clark Evans, Jaymes S. Kenyon, Haiqin Li, Jordan Schnell, Franciano S. Puhales,
Tiziana Cherubini, Weiwei Li, and Man Zhang

January 2026

National Oceanic and Atmospheric Administration
Oceanic and Atmospheric Research
Global Systems Laboratory
Boulder, CO

NOAA Technical Memorandum OAR GSL-77
https://doi.org/10.25923/rahr-sj70

A Description of the MYNN-EDMF Turbulence Scheme

[1]Joseph B. Olson, [2]Wayne M. Angevine, [1]David D. Turner, [2,1]Xia Sun, [2,1,3]Julia M. Simonson, [1]Clark Evans, [2,1]Jaymes S. Kenyon, [2,1]Haiqin Li, [2,1]Jordan Schnell, [4]Franciano S. Puhales, [5]Tiziana Cherubini, [6,3]Weiwei Li, and [2,1,3]Man Zhang

[1]National Oceanic and Atmospheric Administration, Global Systems Laboratory (NOAA/GSL)
[2]Cooperative Institute for Research in Environmental Sciences (CIRES)
[3]Developmental Testbed Center (DTC)
[4]Universidade Federal de Santa Maria (UFSM), Santa Maria, Rio Grande do Sul, Brazil
[5]University of Hawaii at Manoa, Honolulu, Hawaii
[6]National Science Foundation (NSF) National Center for Atmospheric Research (NCAR)

Acknowledgements
The authors would like to thank Dr. Mikio Nakanishi for sharing the original version of the MYNN PBL scheme and offering helpful insight and advice as the scheme was further developed. Funding for this work was provided by many sources, collectively helping to develop a variety of components of the MYNN-EDMF scheme. These agencies/programs include NOAA's Atmospheric Science for Renewable Energy (ASRE) program, the Federal Aviation Administration (FAA), NOAA's UFS-R2O project, and the U.S. DOE Office of Energy Efficiency and Renewable Energy. The views expressed are those of the authors and do not necessarily represent the official policy or position of any funding agency. We are grateful to the NSF National Center for Atmospheric Research Mesoscale and Microscale Meteorology Laboratory, which has been helpful in integrating and maintaining the MYNN-EDMF in their atmospheric models, and specifically grateful for help from Jimy Dudhia, Wei Wang, and Dave Gill. We are grateful for help from the Common Community Physics Package (CCPP) code managers, specifically Grant Firl, Dustin Swales, and Dom Heinzeller. We would like to thank Dr. John Brown for years of insightful conversations on modeling, weather, and turbulence.

National Oceanic and Atmospheric Administration/Oceanic and Atmospheric Research/
Global Systems Laboratory/Earth Prediction Advancement Division
Boulder, Colorado

U.S. Department of Commerce
Howard Lutnick, Secretary

National Oceanic and Atmospheric Administration
Neil Jacobs, Under Secretary of Commerce for Oceans and Atmosphere

Office of Oceanic and Atmospheric Research
Steven Thur, Assistant Administrator

Contents

1. Introduction

The Mellor–Yamada–Nakanishi–Niino (MYNN; Nakanishi and Niino 2001, 2004, 2006, and 2009) turbulence scheme was originally integrated into Advanced Research version of the Weather Research and Forecasting Model (WRF-ARW; Skamarock et al. 2019) v3.1 in 2009. The MYNN was selected for a variety of reasons: (1) improved low-level winds and diurnal cycle of the PBL height in prototype versions of the Rapid Refresh (RAP; Benjamin et al. 2016) v2 and High-Resolution Rapid Refresh (HRRR; Dowell et al. 2022, James et al. 2022) v1, (2) closure constants diagnosed from large-eddy simulations (LES), (3) use of a cloud PDF for the representation of moist turbulent processes, (4) the option to use the level-3 closure, and (5) at the beginning of this integration effort, there were only two PBL schemes in WRF–ARW. After considerable testing and development of the MYNN to better fit within the RAP/HRRR physics suite, it was determined that the performance was deemed sufficient to be chosen as the successor to the Mellor-Yamada-Janjić (MYJ; Janjić 2002) PBL scheme, which was used in RAP v1.

Since that time, the MYNN has undergone many further developments over the years in an attempt to improve bias characteristics in the RAP/HRRR as revealed by extensive model validation for a wide variety of forecast metrics, including near-surface variables, vertical profiles of temperature, winds, and humidity from radiosondes and aircraft data, precipitation, radar reflectivity, cloud ceilings, and downward shortwave radiation (Dowell et al. 2022, James et al. 2022). Many of the improvements were also identified and verified using experimental observations collected during field campaigns (e.g., Olson et al. 2019b). One of the most significant developments of the MYNN was the improved representation of nonlocal mixing with the addition of the mass flux component, making it an eddy-diffusivity (ED)/ mass-flux (MF) (EDMF) turbulence scheme, hereafter referred to as the MYNN-EDMF. There have also been extensions to the ED component, which is a turbulent kinetic energy (TKE)-based scheme when run at closure levels 2.5, 2.6, and 3.0, while turning into total turbulent energy (TTE)-based scheme at level 2.7. The TTE closure level is the newest and least well tested. Each additional closure level beyond level 2.5 provides additional higher-order moments, which are leveraged for representing subgrid-scale clouds (and their cloud-turbulence-radiation interactions), and used for nonlocal mixing at level 3.0. The subgrid cloud representation has matured considerably in recent years as surface shortwave radiation verification results show biases approaching zero. The nonlocal mixing is represented by the MF components, which now includes the representation of both thermal updrafts and negatively buoyant downdrafts produced by cloud-top radiative cooling. The former can produce clouds and represent the impact of latent heat release on updrafts, while the latter can represent subcloud evaporation if the downdrafts penetrate below the cloud base. Both mass-flux components consistently transport all state variables as well as other miscellaneous scalars. We have documented the significant modifications within this memorandum. Closely related modifications to the MYNN surface-layer physics have been documented in Olson et al. (2021).

The MYNN-EDMF has served as the turbulence scheme for NOAA's operational RAP and HRRR forecast systems. Both RAP and HRRR use the WRF-ARW as the dynamical core component. The MYNN-EDMF is also slated for use in the first version of the Rapid Refresh Forecast System

(RRFS), which will replace many of the current regional convective allowing models within the National Weather Service [e.g., NAM-nest (Colbert et al. 2019), HiRes Window] and eventually is expected to be the successor of the HRRR. Version 1 of the RRFS (RRFSv1) uses the Finite-Volume Cubed-Sphere (FV3; Harris et al. 2021) dynamical core linked to the physical parameterizations via the Common Community Physics Package (CCPP; Bernardet et al. 2024). The second version of RRFS (RRFSv2) is planned to use the Model for Prediction Across Scales (MPAS; Skamarock et al. 2012) dynamical core. To centralize the development of the MYNN-EDMF for all applications and modeling frameworks (WRF-ARW, CCPP, and MPAS), the scheme code has been universalized and made accessible in a stand-alone submodule repository (https://github.com/NCAR/MYNN-EDMF), which is then connected to each of the modeling frameworks mentioned above. All future development of the MYNN-EDMF will be hosted in this public-facing submodule repository.

The MYNN-EDMF scheme has been continuously and extensively developed since its last thoroughly documented version (Olson et al. 2019a), as largely been driven by requirements to improve forecast skill in support of the NOAA's National Weather Service (NWS), the Federal Aviation Administration (FAA), and users within private industry. The development efforts have utilized a broad set of conventional and experimental observational data sets, as well as data from large-eddy simulations (LES), to help validate forecasts and shape the fundamental design of the scheme for use at all scales relevant to current or near-future operational forecasting (from $\Delta x = 1$ km to 12+ km). This document overviews the current state of the MYNN-EDMF, including the eddy diffusivity, mass flux (both up- and down-drafts), subgrid cloud representation, numerical procedures, the interactions/coupling between subcomponents, aspects of the practical tuning required for general operational use, the coupling to other physical parameterizations used within a typical physics suite, and a high-level code description. This memorandum serves as a vastly updated description of the MYNN-EDMF, but for the sake of continuity, is patterned after the previous Olson et al. (2019a) technical memorandum.

2. Formulation of the Eddy-Diffusivity Component

The local component of the turbulent vertical fluxes of ϕ (= U, V, θ_{li}, q_x, miscellaneous scalars, and higher-order moments) throughout the entire atmosphere are computed using an eddy-diffusivity approach. This approach uses an eddy-diffusivity coefficient K_H for the thermal and moisture variables and an eddy-viscosity coefficient K_M for the horizontal velocity components. The turbulent fluxes are represented as a product of the local gradient of ϕ (between adjacent model layers) and the coefficient of eddy diffusivity or eddy viscosity (as applicable); i.e.,

$$\overline{w'\phi'} = -K_{H,M}\left(\frac{\partial \phi}{\partial z} - \gamma\right), \qquad (1)$$

where the counter-gradient term, γ, is a function of the higher-order moments when using closure level 3.0 with the updraft mass-flux component inactive. The MYNN-EDMF follows Mellor and Yamada (1982) in that the eddy-diffusivity and eddy-viscosity, K_H and K_M, respectively, are related to q [$q = (2 \cdot TKE)^{1/2} = QKE^{1/2}$, where QKE is an important quantity in the MYNN code], a mixing-length scale (l), and stability functions S_H and S_M, as follows:

$$K_{H,M} = lqS_{H,M}. \quad (2)$$

The stability functions have different forms for closure levels 2.5 and 3.0 (Mellor and Yamada 1982; Nakanishi and Niino 2004), with the additional intermediate closure levels 2.6 and 2.7 leveraging the 2.5-level stability functions. A brief background to each of the individual components of K_H and K_M as well as departures from the components in the original MYNN are described below.

2.1 The TKE Equation

Of foremost importance to any TKE-based eddy-diffusivity PBL scheme is the TKE equation, since TKE is a measure of turbulence intensity and is therefore directly related to the turbulent transport of momentum, heat, and water vapor in the atmosphere (e.g., Stull 1988). As such, TKE is often used in place of vertical-velocity variance in TKE-based PBL schemes. In the MYNN-EDMF, the TKE equation takes the form of:

$$\frac{\partial q^2}{\partial t} = \frac{\partial}{\partial z}\left[lqS_q \frac{\partial q}{\partial z}\right] + P_s + P_b + D, \quad (3)$$

where the advection of TKE by the resolved-scale flow is neglected in Eq. (3), but the scheme itself is designed to function with TKE advection (i.e., Wadler et al. 2023) if the host model is configured to perform TKE advection, as in WRF-ARW and CCPP (described at the end of this section). The first term on the right-hand side of Eq. (3) is the vertical transport term, and P_s, P_b, and D refer respectively to shear production, buoyancy production/destruction, and dissipation. Only slight behavioral changes to the original MYNN are made to the vertical-transport term due to changes in the mixing length (described in the following subsection). The stability function for TKE, $S_q = 3S_M$, remain as in Nakanishi and Niino (2009). This is often larger than the constant $S_q = 0.2$ used in Mellor and Yamada (1982) and Janjić (2002) but smaller than $S_q = 5S_M$ used in Grenier and Bretherton (2001) and Bretherton et al. (2004). The second and fourth terms, relating to the shear production (P_s) and the dissipation (D) of TKE, respectively, also remain as in Nakanishi and Niino (2009).

The third term on the right-hand side of Eq. (3), the buoyancy production/dissipation term P_b, has been modified to include the production of turbulence from the thermal updrafts and the cloud-top cooling represented by their respective mass-flux components (sections 3.1 and 3.2) or the analytical profile method, for which the coupling is described in section 3.3. For both the updraft and downdraft mass-flux components, the TKE production assumes an equilibrium with the dissipation:

$$P_{b\_mf} = \frac{\left|w_{mf}^3\right| a_{mf}}{B_1 l}, \quad (4)$$

where w_{mf} is the mean vertical velocity of all updraft or downdraft plumes and a_{mf} is the total area of the updraft and downdraft plumes. B_1 is a closure constant (= 24) and l is the mixing length, discussed in the following section. The absolute value sign allows the same form to be used for the updrafts or downdrafts.

Similarity-based formulations of the shear and buoyancy production/destruction terms are used at the first model level. This boundary-condition treatment follows the approach described in Puhales et al. (2020), which best matches the form of similarity functions used in the MYNN surface layer scheme (Olson et al. 2021), when the parameter *bl mynn stfunc* = 1. However, by default, *bl_mynn_stfunc* is set to 0, which uses slightly modified form of the Kansas-type formulations (Olson et al. 2021).

Most modeling frameworks have an option to advect the TKE. This option can be used by the MYNN-EDMF because TKE (or QKE) is defined on mass points (middle of layer — not at the interface) unlike many other TKE-based schemes. This definition results in one additional step to average the TKE to the layer interfaces before calculating K_H and K_M, which is thought to have a near-negligible impact, but allows the advection schemes in almost any model to advect TKE like all other scalars defined on mass points. In early versions of the MYNN, the advection of TKE was known to cause numerical instabilities near lateral boundaries, especially when run at level 3.0, so TKE advection has not been activated for use in the operational RAP or HRRR, but has been activated in RRFSv1, which uses the FV3 dynamical core. To activate this option, set the namelist parameter *bl_mynn_tkeadvect* to true (refer to section 8.3).

The MYNN-EDMF includes the contribution of heating due to the dissipation of TKE, which is parameterized as:

$$c_p \frac{\partial T}{\partial t} = d_1 D \ , \qquad (5)$$

where T is the temperature, c_p is the specific heat of dry air at constant pressure, and D is the dissipation of TKE, using the same form as used in Eq. (3). The coefficient d_1 is set to 1.0. This is the same form used in the TKE-based EDMF scheme (Han and Bretherton 2019) currently used within the Global Forecast System (GFS). The heating rate from Eq. (5) is multiplied by the timestep, Δt, and added to the temperature profile prior to computing the tendencies by use of the implicit solver.

Lastly, it is worth mentioning that there have been fixes to the diagnostic TKE budget described in Puhales et al. (2020), which removed some gross approximations and code errors in the original diagnostic output. This work made the output TKE budget much more accurate compared to the actual internal TKE budget, which combines some terms and employs some numerical techniques for efficiency reasons that made the direct output of individual terms complicated.

2.2 Mixing Lengths

The mixing lengths have been revised from the original MYNN PBL scheme, but the original version has been preserved as an option for historical reasons. Below is a brief summary of the original form and updated versions. A namelist parameter *bl_mynn_mixlength* has been added to easily switch between different mixing length formulations (refer to section 8.3). A description of each formulation is as follows:

i. Original form: *bl_mynn_mixlength* = 0

The mixing length, l, is designed such that the shortest length scale among the surface-layer length, l_s, turbulent length, l_t, and buoyancy length, l_b, will dominate. The physical justification is that each length scale is associated with a turbulence-limiting factor, such as static stability, distance from the surface, or the integrated (nonlocal) turbulence within the PBL. After all of the relevant mixing length scales are determined, they must be carefully blended into a single mixing-length profile, which characterizes the mean displacement of a parcel by turbulent eddy mixing at any particular level. To obtain a blended mixing length at each model level, the original MYNN used a linear harmonic average,

$$\frac{1}{l} = \frac{1}{l_s} + \frac{1}{l_t} + \frac{1}{l_b}. \tag{6}$$

As a consequence of the harmonic average, the resultant mixing length is always biased to be smaller than the smallest individual length scale. Alternative blending techniques have been tested in subsequent versions of the MYNN and will be discussed later in this section, but first, we overview the formulation and physical meaning of each individual length scale.

The surface-layer length scale l_s is meant to help regulate the turbulent mixing near the surface, where it is typically the smallest turbulence-limiting factor. In the MYNN, l_s is represented as a function of the surface stability parameter ($\zeta = z/L$), where L is the Obukhov length [$= -u_*^3\ \theta_{v0} / kg(w'\theta')$] and z is the height AGL:

$$l_s = \begin{cases} kz(1 + cns\zeta)^{-1}, & 0 \le \zeta \le 1 \\ kz(1 - \alpha_4\zeta)^{0.2}, & \zeta < 0 \end{cases} \tag{7}$$

where k is the von Karman constant (= 0.4), and the variables "*cns*" and α_4 allow the mixing length to vary with surface stability. Values of α_4 ranging from 10 to 100 allow l_s to become ~O(z) in unstable conditions and values of *cns* ranging from 2.1 to 3.5 reduces l_s to become significantly smaller than kz in very stable conditions. This made the MYNN somewhat unique from earlier PBL schemes, departing from the most commonly used form, $l_s = kz$, which originates from Prandtl's mixing length hypothesis for neutral conditions. Despite this limited region of the validity for using kz, this approximation is nonetheless has been used across the entire spectrum of stability in many older (pre-2010) PBL schemes. The general form of l_s has remained the same in the MYNN-EDMF, but the constants *cns* and α_4 (Fig. 1) have been modified relative to the original MYNN (Nakanishi and Niino 2009) to improve low-level wind speeds.

The general form of the turbulent length scale l_t is taken from Mellor and Yamada (1974) but is modified to become larger in magnitude:

$$l_t = \alpha_1 \frac{\int_0^\infty qz\, dz}{\int_0^\infty q\, dz}, \tag{8}$$

where q is defined above and $\alpha_1 = 0.23$ as opposed to 0.10 in Mellor and Yamada (1974), which helped to alleviate the common undermixing found in older TKE-based PBL schemes. This mixing length scale typically dominates in the middle and upper portion of a convective boundary layer and can vary from 10–50 m in stable conditions to 100–500 m in unstable conditions; therefore, l_t can be thought of as an approximation for the size of the mean turbulent eddy in the PBL. Note

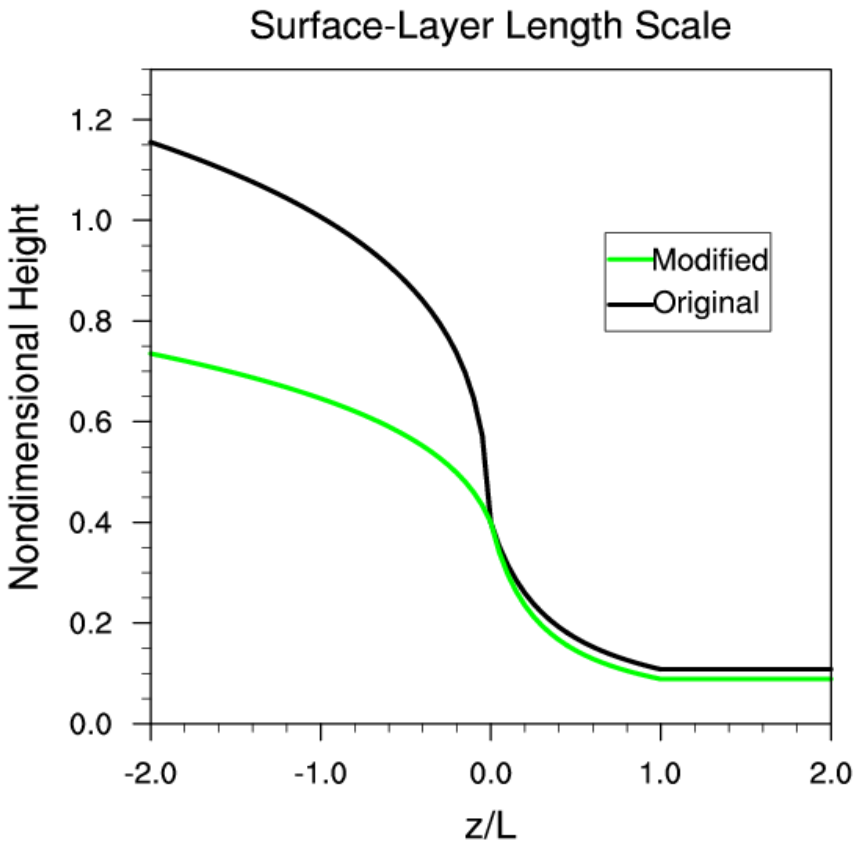

Figure 1. Modified (green) and original (black) surface-layer length scales. The green line shows Eq. 7 with updated values of cns = 3.5 and α_4 =10, while the black line has original values of cns = 2.7 and α_4 =100. A non-dimensional height of 0.4 is equivalent to $l_s = kz$, strictly valid only at neutral conditions (z/L = 0).

that in the original MYNN, this form was integrated from the surface to the top of the model atmosphere, taking into account TKE that is well above the PBL. This caused l_t to be occasionally diagnosed in excess of 2000 m, resulting in spuriously large TKE and even some infrequent model crashes. This was revised (for all mixing length options) to only integrate to the top of the PBL height plus an estimated entrainment layer (described more thoroughly below).

The buoyancy length scale l_b is:

$$l_b = \alpha_2 \frac{q}{N}\left[1 + \alpha_3 \left(\frac{q_c}{l_t N}\right)^{1/2}\right] \qquad (9)$$

where the Brunt-Väisälä frequency, $N = [(g/\theta_0)\partial\theta_v/\partial z]^{1/2}$, and $q_c = [(g/\theta_0)\langle w'\theta'_v\rangle\, l_t\,]^{1/3}$ is a turbulent velocity scale, similar to the convective velocity scale (w_*), but uses l_t instead of z_i. l_b is the length scale that primarily regulates the magnitude of the mixing lengths in stable conditions in the upper convective boundary-layer and free atmosphere. It not only regulates the strength of the vertical diffusion in the stable boundary layer but also impacts the entrainment between the boundary-layer and the free atmosphere (Lenderink and Holtslag 2000). The coefficient α_2 is important for modulating the size of l_b, and varies widely in the literature from 0.2 (Lenderink and Holtslag 2004) to 0.25 (Mahrt and Vickers 2003; they used σ_w/N) to 0.53 (Galperin et al. 1988; Furuichi et

al. 2012) to 0.71 (Abdella and McFarlane 1997) to 1.0 (Nakanishi and Niino 2004 and 2009) to 1.69 (Nieuwstadt 1984; they also used σ_w/N). Not surprisingly, Lock and Mailhot (2006) suggest that the optimal value for α_2 may vary with boundary-layer regimes. This wide variety of values chosen for α_2 in the literature does not necessarily reflect its range of uncertainty; rather, it can vary in different PBL schemes due to other compensating factors, such as choices of constants used to regulate the dissipation rate of TKE. Many values of α_2 have been tested within the MYNN and this parameter has been decreased from 1.0 to 0.65 to 0.3 in successive revisions (discussed further below).

The second term in the brackets of Eq. (9), hereafter termed the buoyancy enhancement term (BET), acts to enlarge l_b for conditions with a positive surface heat flux ($\zeta < 0$), which helps to reduce the impact of l_b on the harmonically averaged mixing length when buoyancy effects should be minimized. This provides a mechanism for l_b to vary with boundary-layer regimes without needing to vary α_2, but introduces a new amplification factor α_3. However, the dependence upon the surface heat flux in the BET is questionable since the surface fluxes may have little relevance to the turbulence well above the boundary layer. The exception would be in a deep convection regime, but mixing in this regime should be handled by a convection scheme and/or resolved convective plumes.

ii. The nonlocal revision: *bl_mynn_mixlength* = 1 (default)

A set of changes made to the mixing lengths were needed to alleviate problems in the original version. Specifically, these problems were:

(1) the excessively large magnitudes of l_t (mentioned above),
(2) the dependency of l_b upon a local calculation of N can give rise to singularities in unstable layers and, since l_b is a function of l_t, which is only valid in the boundary layer, the original form of l_b should either only be used below z_i or the BET must be removed for use in the free atmosphere,
(3) related to the changes in the stability functions (discussed later in section 2.3), a reduction in mixing was required to reduce a high 10-m wind speed bias present in both nocturnal and daytime conditions,
(4) a lack of coupling between the subsequently added mass-flux components and the eddy diffusivity component, and
(5) a lack of tuning for tropical cyclones (or high wind speed conditions in general).

The first problem required a modification to the depth of the integration of l_t in Eq. (8). Instead of integrating from the surface to the top of the model atmosphere, it is now only integrated to the top of the PBL (denoted z_i), plus a transition layer (or entrainment layer) depth $\Delta z = 0.3 z_i$ (Garratt 1992). The original MYNN operated independently of z_i; that is, z_i was not used as an independent variable to diagnose other quantities within the scheme. This modification requires an accurate diagnostic calculation of z_i (described later in section 7.1).

An attempt to rectify the problems with l_b was to implement a nonlocal mixing-length formulation from Bougeault and LaCarrere (1989; hereafter known as the "BouLac" mixing length, l_{BL}). The algorithm for the BouLac mixing length involves looping upward and downward until vertical distances of displacement l_{up} and l_{down} are found which represent the distances a parcel can be

vertically displaced given a local amount of TKE within an ambient stratification. Then, an average of l_{up} and l_{down} is taken as $l_{BL} = (l_{up}^2 + l_{down}^2)^{1/2}$. Since this formulation is nonlocal in design, it is capable of diagnosing mixing lengths in unstable layers, such as breaking mountain waves, so it nicely addresses the problems associated with Eq. (9). To restrict the use of l_{BL} to the free atmosphere and preserve the original MYNN mixing-length formulation in the boundary layer, a blending approach is adopted. A transition (or entrainment) layer is defined where the original buoyancy length scale, l_b, is used below z_i and l_{BL} is used above:

$$l_b = l_b(1 - W) + l_{BL}W \tag{10a}$$

$$W = 0.5tanh\left(\frac{z_i + \Delta z}{\Delta z/2}\right) + 0.5 \tag{10b}$$

This formulation makes the buoyancy-length scale equal to l_b below z_i, about 50% each at the top of the entrainment layer ($z_i + \Delta z$), and equal to l_{BL} above $z_i + 2\Delta z$. The specific depth of the layer used in this blending approach has little impact on the behavior of the turbulent mixing near the PBL top.

Two simple tuning adjustments have been made to counter other required changes and reduce biases diagnosed in the operational RAP/HRRR models. The first adjustment was to reduce the magnitude of the mixing in stable conditions, which was required after a change made to the closure constant A_2 to fix a negative TKE problem (described later in section 2.3). This change, in consultation with Dr. Mikio Nakanishi, reduced the coefficient α_2 (associated with l_b) from 1.0 to 0.65, but was later reduced further to 0.3. Reducing α_2 helped improve low-level jet structure and the maintenance of mountain-valley cold pools. Tests at values below 0.3 began to show signs of under-diffusive behavior. A second modification reduced a high 10-m wind speed bias in the RAP/HRRR during the daytime. It was found that a reduction of α_4 from 100 to 20 sufficiently reduced l_s in unstable conditions, which reduced the mixing of momentum down to the surface during the daytime, greatly improving the simulated low-level wind speeds.

To improve the coupling of the mass-flux component with the eddy-diffusivity component beyond the simple addition of TKE production by the mass-flux schemes (discussed in the previous section), the buoyancy mixing length scale described by Eq. (9) is modified to

$$l_b = max\left(\alpha_2 \frac{q}{N}\left[1 + \alpha_3 \left\{\frac{q_c}{l_t N}\right\}^{\frac{1}{2}}\right], \alpha_6 \frac{M}{N}\right), \tag{11}$$

where M is the mass flux (= total area of plumes × mean velocity of plumes; described in section 3) from the updrafts and downdrafts, if present, and $\alpha_6 = 50$. This was added with the assumption that the mixing lengths in grid cells with stable stratification and penetrating (nonlocal) updrafts or downdrafts present should have increased mixing lengths, which will help reduce the local dissipation of TKE.

Some tropical cyclone-specific tuning of the mixing lengths was added to improve a low-intensity bias found in earlier versions. These modifications are only active over water grid points and are implemented in a way that minimizes their impact in non-tropical cyclone conditions, so they are used in all configurations. Two modifications were implemented:

(1) a maximum magnitude of l_t (= 400 m) was added, and
(2) α_3 in the second term in the brackets of Eqs. (9) and (11), is tapered down 50% between 20 and 70 m s^{-1}.

In addition, the harmonic-averaged blending of the individual mixing length scales was modified to obtain more control of the magnitude of the mixing lengths. The linear harmonic averaging, as it exists in Eq. (6), can result in dramatically reduced mixing lengths, less than 50% in magnitude of the smallest component. Alternative blending techniques were investigated (e.g., Chen and Bryan 2021), but some degradation was found outside of tropical cyclone environments. Instead, the problem of the small-biased averaged mixing length was alleviated by reducing the number of components used in the harmonic average from three to two, using only l_s and l_t, as was proposed by Blackadar (1962), but included a *MIN* function to account for the effects of buoyancy represented by l_b:

$$l_{meso} = MIN\left[\frac{1}{\frac{1}{l_s}+\frac{1}{l_t}}, l_b\right]. \quad (12)$$

This method was originally proposed by Dr. Mikio Nakanishi (personal communication). This form makes the mixing length formulation more *z-less* (not dependent on the distance to the surface) in nature (Nieuwstadt 1984, Ha and Marht 2001) when the buoyancy effects become the turbulence-limiting factor (l_b becomes the smallest length scale). In this statically stable situation, l_s and l_t do not impact l (*z-less*); only the local stability and turbulence (l_b) controls l.

This set of modifications completes the description of the nonlocal mixing-length revision to the MYNN and can be used by setting the namelist option *bl_mynn_mixlength* to 1. This version is recommended and is active by default. A comparison between the mixing length options (Fig. 2) shows that option 1 generally results in smaller mixing lengths, TKE, and eddy diffusivity than the original option 0 in convective conditions, but can produce larger mixing lengths above the PBL height due to the nonlocal BouLac mixing length.

iii. The local version: *bl_mynn_mixlength* = 2

A second mixing length formulation maintains the advances in option 1 (i.e., coupling to the mass-flux component and improved performance in stable conditions), but attempts to improve the computational efficiency and explore the potential benefits of alternative blending options. This objective to reduce the computational expense resulted in a replacement of the BouLac mixing length that was added for option *bl_mynn_mixlength* = 1.

The two primary differences between options 1 and 2 are:
(1) Option 2 uses the squared-blending from Chen and Bryan (2021):

$$\frac{1}{l^2} = \frac{1}{l_s^2} + \frac{1}{l_t^2} + \frac{1}{l_b^2}, \quad (13)$$

which better preserves the magnitude of the smallest length scale compared to Eq. (6) and has been shown to perform well in idealized tropical cyclone simulations. However, this

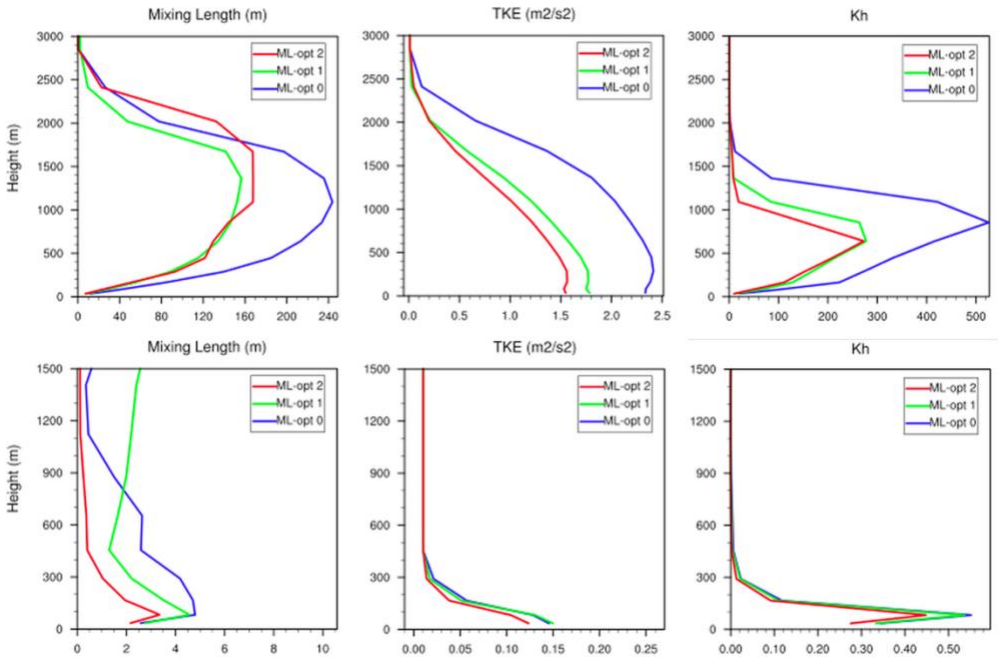

Figure 2. A comparison of each mixing length option (colors) for mixing lengths (left), TKE (center), and eddy diffusivity (K_H, right) for convective conditions at 1800 UTC (top) and stable conditions at 0900 UTC (bottom) over a region in northern Minnesota in a HRRR forecast initialized at 0600 UTC 26 August 2016.

blending technique results in generally larger mixing lengths, which can result in increased mixing that will systematically degrade 10-m wind speeds and low-level jets unless some counter-tuning is performed. We can limit these degradations by reducing α_4 in Eq. (7) from 20 to 5, which reduces the surface-layer mixing lengths in unstable conditions. Further reduction in α_2 in Eq. (11) can help reduce the overmixing in stable conditions, but this does not seem to result in systematic improvements to low-level wind. Additional constraints to the Prandtl number (discussed later in section 2.3) also seem to help improve stable low-level jet structures. In summary, this change has positive attributes but also carries consequences if not accompanied by some minor recalibration.

(2) Improvements to the computational efficiency of the mixing length required replacing the BouLac with an alternate length scale that is not prone to singularities in unstable layers. The cloud-specific length scale of Teixeira and Cheinet (2004) provides a much more computationally efficient estimate and is not prone to singularities:

$$l_b = \tau(TKE)^{1/2} . \qquad (14)$$

In the convective boundary layer, Deardorff (1970) suggests that the time scale τ is proportional to z_i/w_*, where z_i is the PBL height and w_* is the convective velocity scale:

$$\tau = 0.5\frac{z_i}{W_*} = 0.5\frac{z_i}{(\frac{g}{\theta_0}z_i\overline{w'\theta'})^{1/3}} . \qquad (15)$$

However, having w_* inversely proportional to τ is somewhat counterintuitive since a larger w_* is more likely to be associated with larger turbulent structures, which would be associated

with larger eddy turnover timescales. Therefore, we depart from this form used in Teixeira and Cheinet (2004) and instead replace it with the following form:

$$\tau = c_\tau \frac{w_*}{g}, \tag{16}$$

where c_τ is a time constant set to 1000 seconds. Above z_i, τ is set to 50 seconds. This TKE-based form is used in place of the original l_b Eq. (11) in neutral or unstable layers, when N becomes non-positive.

The comparison of the mixing lengths (Fig. 2) shows that mixing length option 2 behaves similarly to option 1 in convective conditions but can be slightly smaller in stable conditions, especially above the PBL height, where the local method produces magnitudes generally smaller than the nonlocal BouLac length scale.

iv. Scale-adaptivity applied to all *bl_mynn_mixlength* options

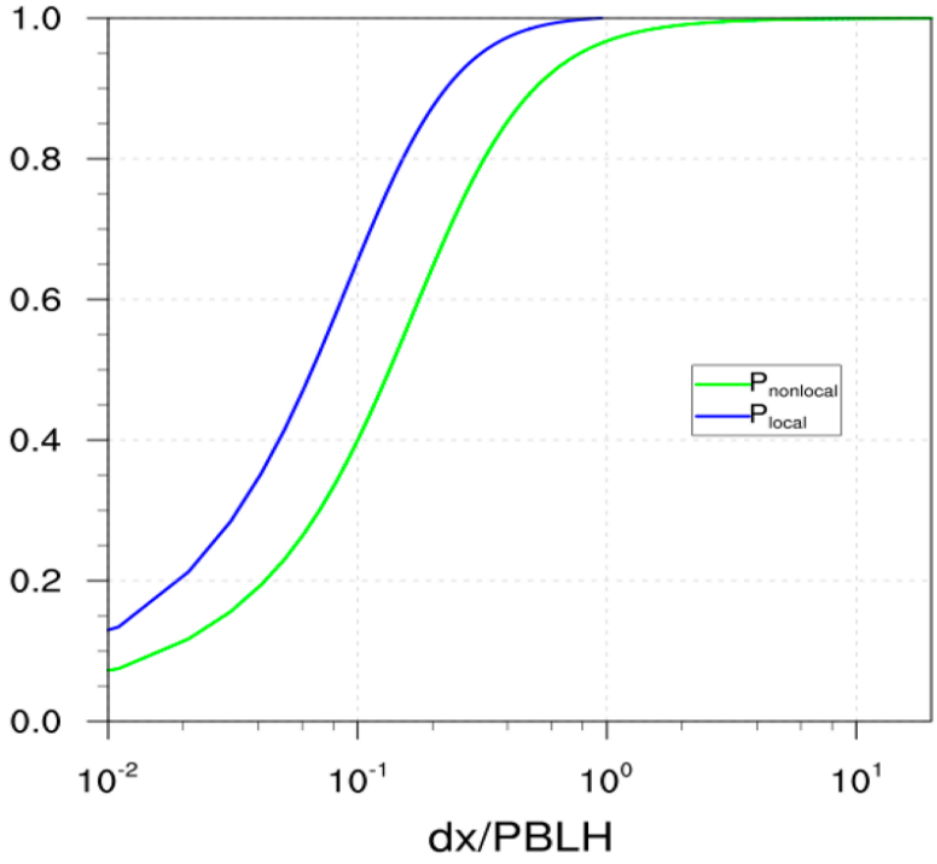

Figure 3. Tapering functions used for nonlocal processes (green) and local processes (blue). The local function is taken from Honnert et al. (2011), representing the variation of parameterized TKE in the boundary layer. The nonlocal function is taken from Shin and Hong (2013), representing the variation of parameterized TKE in the entrainment zone. Following the results from Angevine et al. (2020), which suggested the tapering needed to be minimized in the upper portion of the grey zone, the functions were phase shifted by inputting 2.5Δx (instead of Δx) to acknowledge the impact of the effective resolution as opposed to the model grid resolution.

Lastly, after all length scales are computed and blended into a vertical profile, another scale-adaptive blending function is applied to the mixing lengths to ensure that a relevant form is used for any particular model configuration within the boundary-layer grey zone (2000 m > Δx > 200 m). This idea is taken from Cuxart et al. (2000) and Ito et al. (2015), where a "mesoscale" form of mixing lengths (as described above) is blended with a form more appropriate for LES. The similarity functions *P* from Honnert et al. (2001) and Shin and Hong (2013) suggest that this blending should take place between 2000 m > Δx > 200 m, but Honnert et al. (2001) caution against the direct use of their functions in any particular model code without rigorous testing. Angevine et al. (2020) and Shin and Hong (2013) both show that the MYNN-EDMF has a natural tapering of the turbulent mixing within the grey zone and can actually perform worse if similarity functions are applied to overly reduce parameterized turbulent mixing within the grey zone. Therefore, the approach taken in the MYNN-EDMF is to concentrate the tapering, or more accurately, the *transitioning*, of the mixing lengths in the lower end of the grey zone (between 600 and 200 meters). We emphasize the word transition over tapering when applied to the eddy-diffusivity component because the modified similarity functions are used to perform a blending from the *mesoscale* mixing lengths (calculated in option *bl_mynn_mixlength* = 0-2) with a purely-local *LES* mixing length, as opposed to simply tapering the mixing lengths to zero as Δx $\rightarrow$ 0 (Fig. 3; blue curve). The LES mixing length is: $l_{\mathrm{LES}} = 0.25*\Delta z$. Then the blending is as follows:

$$l = l_{meso}P_{local} + l_{LES}(1 - P_{local}). \quad (17)$$

This makes the eddy-diffusivity component of the MYNN-EDMF *partially scale-adaptive* with respect to the model grid spacing. The authors would strongly argue that to fully achieve scale-adaptive functionality, the 1-D mixing scheme should also transform to a 3-D mixing scheme like that used in LES configurations (Kurowski and Teixeira 2018), but this extension is only in the planning stages (thus will be implemented in a future version of the MYNN-EDMF).

2.3 Stability Functions

In the Mellor-Yamada framework, the level 2.0 stability functions S_H and S_M are functions of the gradient Richardson number, *Ri*, and the closure constants, which have been tuned to best match LES results as in Nakanishi and Niino (2004, 2009). All of the closure constants in the updated MYNN-EDMF remain the same, with the exceptions of A_2, C_2, and C_3.

Kitamura (2010) introduced a simple modification to the MYNN based on the method proposed by Canuto et al. (2008). This modification applies a stability-dependent relaxation to the original closure constant A_{2_orig}, such that it becomes a closure *variable* in statically stable conditions (Ri > 0):

$$A_2 = \frac{A_{2\_orig}}{1+\max(Ri,0.0)} \quad (18)$$

In both the original MYNN and the MYNN-EDMF, the mixing length for vertical heat transport is given as $A_2 l$ (where l is the mixing length). Hence, this reformulation of A_2 causes the mixing lengths used for the turbulent heat flux to decrease with stronger static stability but does not affect

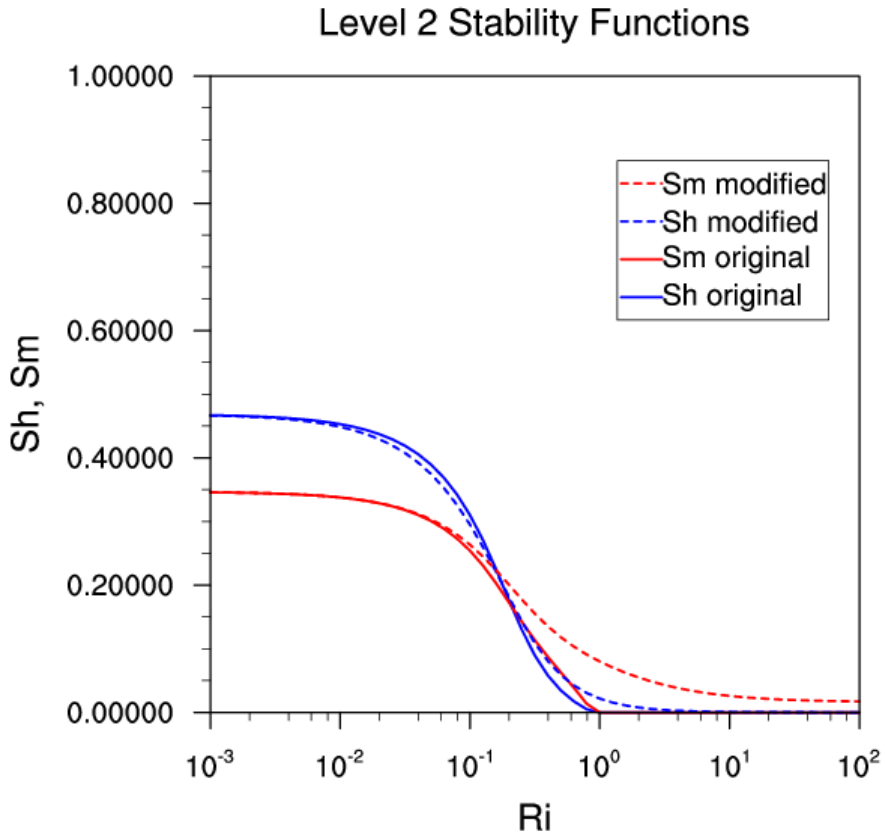

Figure 4. Original (solid) and modified (dashed) Level 2 stability functions for momentum (red) and heat (blue).

the turbulent mixing of momentum. This modification was shown by Kitamura (2010) to remove the critical Richardson number, Ri_c, allowing small finite momentum mixing to exist as $Ri \rightarrow \infty$, (Fig. 4) as argued for by various turbulence researchers (i.e., Galperin et al. 2007; Zilitinkevich et al. 2007; Canuto et al. 2008). This modification does not transform the MYNN into a total turbulent energy (TTE) scheme, like Mauritsen et al. (2007), Zilitinkevich et al. (2007), and Angevine et al. (2010), but does allow it to inherit some TTE scheme characteristics; namely, the Prandtl number (Pr; the ratio of the momentum mixing to heat mixing, K_M/K_H) for local mixing can become very large in stable conditions, and the scheme no longer has a critical Ri for momentum. This modification has existed in the MYNN-EDMF since approximately 2015 (WRF-ARWv3.7) and is activated by default.

Kitamura (2010) cautioned that this modification may require subsequent adjustments to reduce the closure constants C_2 and C_3. After consulting with Dr. Mikio Nakanishi, we revised C_2 and C_3 to 0.729 and 0.34, respectively, which fall within the range suggested by Gambo (1978); however, test simulations revealed that the removal of Ri_c resulted in increased mixing in stable conditions, spurring efforts to further reduce the mixing-length scales in stable conditions as described in section 2.2.

A second effort to reduce overmixing in stable conditions was to impose an upper bound on Prandtl number in stable conditions taken from Kondo et al. (1978):

$$\mathrm{Pr}_{max} = MIN[6.873*Ri + 1/(6.873*Ri), 5]. \quad (19)$$

This limit only impacts the strength of momentum mixing, since heat mixing is already very small in stable conditions.

2.4 Closure Levels

A namelist parameter, *bl_mynn_closure* (real), has been added to configure the closure level for the MYNN-EDMF. This determines how many higher-order moments will be prognosed, which stability functions will be used, and how the standard deviation of the saturation deficit is calculated when using the subgrid cloud scheme (*bl_mynn_cloudpdf* = 2; described in section 4). For levels 2.7, it also determines how the eddy viscosity, K_M, is calculated (discussed below). This subsection briefly overviews each closure level option, as summarized in Table 1:

i. Level 2.5: *bl_mynn_closure* $\leq$ 2.5

At level 2.5 (a.k.a. closure *order* 1.5), only TKE is prognosed. Because of this, an important variable used within the cloud Probability Density Function (PDF), the moisture variance q'^2 [not to be confused with $(2 \cdot TKE)^{1/2}$], will only be diagnosed. This will cause it to vary more stochastically in time and space, making it less optimal for use in the calculation of the subgrid clouds. There have been some bounds added to the code to keep it within a reasonable range, so the use of any of the cloud PDF options is still possible, but the simulated clouds (and radiative interaction) may rely more heavily on imposed limits. Note that running at level 2.5 does not automatically activate TKE advection. Setting *bl_mynn_tkeadvect* = true will activate TKE advection (in WRF and CCPP). This closure uses the level 2.5 stability functions and does not use the counter-gradient terms, so it will rely on the mass-flux components for nonlocal mixing.

ii. Level 2.6: 2.5 < *bl_mynn_closure* < 2.7 (default option)

At level 2.6 (a.k.a. closure *order* 1.6), both TKE and q'^2 are prognosed. This closure was created primarily for the benefit of the subgrid-cloud property estimations by the cloud PDFs because q'^2 is the most important input and it generally evolves more realistically in time and space when prognosed, making it less reliant upon imposed limits. As of now, there is no configuration option to conveniently control the advection of q'^2 in any model framework, but this may be explored soon. This closure level leverages the level 2.5 stability functions and does not use the counter-gradient terms, so it will rely on the mass-flux components for nonlocal mixing.

iii. Level 2.7: 2.7 $\leq$ *bl_mynn_closure* < 3.0

At level 2.7 (a.k.a. closure *order* 1.7), TKE, q'^2, and θ'^2 are prognosed. This setting is also ideal for use within the cloud PDFs, which will leverage both q'^2 and θ'^2 to compute the subgrid cloud properties, but the additional impact of θ'^2 is secondary. The primary reason for making this closure level is to experiment with a fully total turbulent energy (TTE) configuration, since θ'^2 can be used to diagnose turbulent potential energy (TPE) following Machulskaya and Mironov

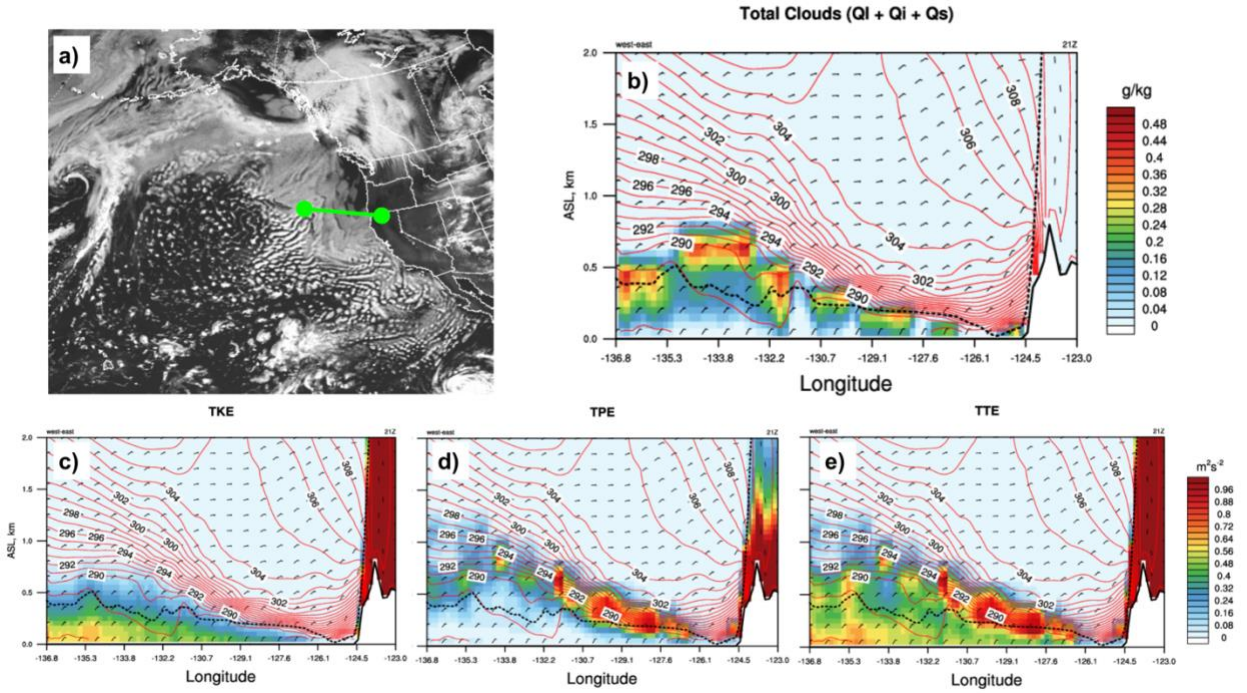

Figure 5. WRF Model simulation of a stratocumulus event initialized at 0600 UTC 26 Aug 2016, forecast hour 15, valid at 2100 UTC. (a) upward shortwave at top of model. The other panels are vertical cross-sections oriented along the green line in (a) showing potential temperature (red contours), wind barbs, and (b) total clouds, (c) TKE, (d) TPE, and (e) TTE (=TKE+TPE).

(2020). In this case, TPE is added to TKE when computing the K_H. This seems to have a small overall impact, likely because the MYNN-EDMF has already been modified to have some traits of a TTE scheme (see section 2.3). The overall impact is to produce the *potential* increase in momentum mixing in stable conditions. An example of how TPE can complement TKE in a stratocumulus environment is shown in Fig. 5. As of now, there is no configuration option to conveniently control the advection of q'^2 or θ'^2 in any model framework, but this may be explored soon. This closure level leverages the level 2.5 stability functions and does not use the counter-gradient terms, so it will rely on the mass-flux components for nonlocal mixing.

iv. Level 3.0: *bl_mynn_closure* $\geq$ 3.0

At level 3.0 (a.k.a. closure *order* 2.0), TKE, q'^2, θ'^2, and $q'\theta'$ are all prognosed. In theory, this should be the most robust configuration for use within the cloud PDF as it will leverage all higher-order moments to compute the subgrid cloud properties. This configuration is not the default setting because it contains its own representation of nonlocal mixing by use of counter-gradient terms, which are based off of the higher-order moments. This older approach to represent the impacts of nonlocal mixing is less sophisticated than the explicit representation of penetrating convective plumes by a mass-flux component. This closure level is kept similar to its original form in that it (a) will not run as a TTE scheme (until further testing is performed), and (b) will rely on the counter-gradient terms for nonlocal mixing when the mass-flux components are deactivated (*i.e.*, *bl_mynn_edmf* = 0 and *bl_mynn_edmf_dd* = 0), which is advised, in order to avoid duplicate representation of nonlocal processes. As of now, there is no configuration option to conveniently control the advection of q'^2, θ'^2, or $q'\theta'$ in any model framework, but this may be explored soon.

Table 1. List of closure level options, the higher-order moments prognosed at each level, and a brief description of the main functionality.

Option	Variables prognosed	Description
bl_mynn_closure = 2.5	TKE	Standard TKE scheme with mass-flux component and subgrid clouds. Uses the level 2.5 stability functions.
bl_mynn_closure = 2.6	TKE, q'^2	Leverages better q'^2 behavior for cloud PDF. Uses the level 2.5 stability functions. (default)
bl_mynn_closure = 2.7	TKE, q'^2, $\boldsymbol{\theta}'^2$	Leverages $\boldsymbol{\theta}'^2$ for turbulent potential energy (TPE), now a TTE scheme. Uses the level 2.5 stability functions.
bl_mynn_closure = 3.0	TKE, q'^2, $\boldsymbol{\theta}'^2$, $q'\boldsymbol{\theta}'$	Uses countergradient method **or** MF for nonlocal mixing. Uses the level 3.0 stability functions.

The advection of the covariance term is complicated since it can be both positive and negative, so simply advecting it without special treatment is not advised. This closure level uses the level 3.0 stability functions.

The difference in computational cost between closure levels is typically small, < 3% of the scheme run time, depending on the other configuration options. The advection of each additional higher-order moment may cause larger increases in computational cost, if invoked, compared to the cost of prognosing additional higher-order moments.

3. Formulation of the Mass Flux/Nonlocal Mixing Components

Eddy-diffusivity schemes perform reasonably well in stable boundary layer applications but cannot adequately describe the nonlocally-driven turbulent fluxes in the upper portion of the convective boundary layer or represent the clouds produced by convective plumes. Additional nonlocal components such as counter-gradient terms or explicit entrainment parameterizations must be added to eddy-diffusivity schemes to represent the nonlocal mixing. The original MYNN PBL scheme has some representation of nonlocal mixing when run at level 3, which makes use of counter-gradient flux terms; however, the level 2.5 model is primarily a local-mixing scheme (when not considering nonlocal aspects of the mixing length formulation, as discussed in section 2).

A more suitable approach for the representation of nonlocal mixing in convective boundary layers is the mass-flux method. Siebesma et al. (2006) have shown that this approach has strong advantages over the more traditional counter-gradient approach, especially in the entrainment layer. Mass-flux schemes can represent the nonlocal turbulent transport by thermal plumes for both dry and cloud-topped boundary layers. Boundary layer thermals or plumes can be thought of as the invisible roots that produce shallow cumulus clouds (Lemone and Pennell 1976). Therefore,

mass-flux schemes provide a way to represent these plumes and allow for a direct coupling of subcloud convective cores with the cloud layer above. The inclusion of a mass-flux formulation within the MYNN PBL scheme moves it into the class of eddy-diffusivity mass-flux (EDMF) schemes as well as the category of nonlocal mixing schemes. One major design advantage the EDMF approach is that it allows for some of the turbulent transport of heat, moisture, and momentum to be performed by the mass-flux scheme in convective conditions, requiring less of the local turbulent mixing to be performed by the eddy-diffusivity component. This allows the eddy-diffusivity portion of the MYNN-EDMF to specialize in treating the stable boundary layer, while the mass-flux portion helps to improve the representation of nonlocal mixing in unstable conditions.

The MYNN-EDMF is used in operational regional forecast systems (HRRR, RAP, and RRFS) that are responsible for providing a wide range of forecast guidance, such as the timing and location of severe convection, cloud ceilings, precipitation, and low-level winds, so improvements to the representation of strong thermals in the convective boundary layer must not come at the expense of these fields. Specific design features are added to the mass-flux scheme to help generalize its applicability to any relevant weather regimes. Furthermore, since the RAP/HRRR physics suite is often used for much higher resolution (sub-kilometer) applications in support of major field studies, the mass-flux scheme must be designed to perform well at very small horizontal grid spacing (~500 m), which delves well into the grey zone of shallow-convection modeling. This requires the integration of scale-adaptive flexibility into the mass-flux component, such as through the frameworks proposed by Neggers (2015) and Sušelj et al. (2013) that inspired the design of this scheme. The following subsections describe the overall design, scale-adaptive features, and configuration options for the nonlocal component of the MYNN-EDMF.

3.1 Surface-Forced Thermal Updrafts

The blending of the mass-flux scheme with the eddy-diffusivity scheme requires a partitioning of the total turbulent fluxes, such that the vertically coherent convective updrafts represented by the mass-flux scheme cover a fraction of the model grid cell, a_u, and the rest of the grid cell, $1-a_u$, contains the small-eddy mixing associated with the eddy-diffusivity scheme. We will formally define a_u later. With this approximation, the total turbulent fluxes (mixing and transport) of any arbitrary variable ϕ can be represented as three terms following Siebesma and Cuijpers (1995):

$$\overline{w'\phi'} = a_u\overline{w'\phi'}^{u} + (1-a_u)\overline{w'\phi'}^{e} + a_u(w_u-\bar{w})(\phi_u-\phi_e) \qquad (20)$$

where the sub- and superscripts u and e refer to the area of convective updrafts and environment, respectively. For the rest of this description, we ignore the sub- and superscripts e and assume that all unscripted variables describe the environment (given by the model grid cell mean). The first term on the r.h.s. of Eq. (20) represents the small-eddy mixing within the updrafts, which is typically neglected with the assumption that $a_u \ll 1$. The second term represents the small-eddy mixing in the nonconvective plume portion of the grid cell, which is represented by the eddy-diffusivity scheme. The third term of the r.h.s. of Eq. (20) represents the nonlocal turbulent transport from the convective mass flux, defined as $M \equiv a_u(w_u - w)$. This term can replace the counter-gradient term, γ, in Eq. (1), which can now be approximated as:

$$\overline{w'\phi'} \cong -K_{h,m}\frac{\partial \phi}{\partial z} + M(\phi_u - \phi). \quad (21)$$

In the MYNN-EDMF, the second term in Eq. (21) is represented with a multiplume approach, following Neggers (2015) and Sušelj et al. (2013), so summation notation is more appropriate:

$$\overline{w'\phi'} \cong -K_{h,m}\frac{\partial \phi}{\partial z} + \sum_{i=1}^{n} M_i(\phi_{u_i} - \phi)\,, \quad (22)$$

where i represents an individual plume and n is the total number of plumes. Like the eddy-diffusivity parameterization that is meant to represent an ensemble of turbulent eddies of various sizes, the approach of Neggers (2015) attempts to represent a variety of convective plumes of different sizes. We adopt a similar approach here. In the past (pre-2023), we used a variable number of plumes, but this has been changed to use a constant number (eight plumes), where the smallest plume is assigned a diameter of 300 m and the largest plume diameter varies with the environmental conditions (discussed in the following paragraph). This modification was made for (a) a computational speed up by allowing to more loops to vectorize after being fixed to a constant dimension and (b) a continuously varying incremental diameter between each plume helps to eliminate the numerical noise associated with discretely adding/removing plumes when the environmental conditions change. But just like before, each plume can be dry or, if penetrating above the lifting condensation level (LCL), can condense and produce shallow cumulus clouds. The different plume diameters result in different entrainment rates ε_i, as defined by Tian and Kuang (2016), but modified to also take into account the impact of the ambient TKE on the entrainment rate:

$$\varepsilon_i = \frac{c_\varepsilon}{w_i d_i} \quad (23)$$

where w_i is the vertical velocity and d_i is the diameter of each plume i. The constant c_ε, which was previously 0.33, is now allowed to vary between 0.27 and 0.34 according to the mean TKE (or QKE = 2×TKE) in the PBL:

$$c_\varepsilon = 0.21(\overline{QKE_{PBL}})^{1/2} \quad (24)$$

which is larger than the value (0.23) estimated by Tian and Kuang (2016) in LES experiments. In their study, they defined d as the distance to the edge of the cloud as opposed to the plume diameter, so a slightly larger value better fits our definition of d. This diameter-dependent entrainment rate allows each plume to evolve differently, thus attempting to represent a broad range of thermals in a convective boundary layer.

Determining the maximum plume diameter involves taking physical, numerical, and practical tuning aspects into consideration. Below, we outline four criteria for selecting the maximum plume diameter:

1. Although the total number of plumes is fixed to eight, not all meteorological conditions are associated with large plumes. A good example is midmorning (during a typical diurnal progression), when the surface heat fluxes become positive (directed upward) but the boundary layer is still only beginning to build. In this condition, only small plumes are beginning to organize; the largest plumes approximately scale to the depth of the subcloud-layer height (Neggers et al. 2003). In such conditions, we approximate the maximum plume

width to scale closely with the boundary layer height, z_i, as $d_{max} = 1.1z_i$, up to a maximum of 1000 m. The maximum of 1000 m is chosen to limit the size to plausible (but still large) shallow convection. Plumes of larger diameter are likely associated with mid-level congestus or deep convection. This makes the MYNN-EDMF s*cale-adaptive with respect to the relevant scales of the meteorological conditions*.

2. An additional limitation on the maximum plume width is exercised in the case where there exists a cloud ceiling, defined as a model layer with cloud fraction in excess of 50%. In this case, the maximum plume width d_{max} is set to a fraction of the ceiling height z_c. The fraction is set to 0.5 over land and 0.8 over water. The surface forcing of turbulence is generally muted by the shading of clouds in high cloud cover regimes, but there can be some exceptions, so this may be considered more a practical tuning constraint than physically realistic constraint, but it helps regulate the strength of the plumes so that stratus clouds are not so easily mixed out.
3. The horizontal grid spacing Δx (in meters) also regulates d_{max}. We imposed a limit on the maximum plume width to be less than $d_{max} = 1.2\Delta$x, so there is no attempt to parameterize plumes greater than what can be only partially resolved. This makes the MYNN-EDMF *scale-adaptive with respect to the model grid spacing*.
4. The surface buoyancy flux, H_{sfc}, is also used to regulate d_{max}. The purpose is to provide a "soft triggering" mechanism, as discussed in Neggers et al. (2009), allowing the plume strength to gradually increase as the surface forcing increases. We use a hyperbolic tangent function:

$$d_{max} = 1000\left[\frac{3}{5}\tanh\left(\frac{H_{sfc}-H_0}{\Delta H}\right)+\frac{1}{2}\right], \qquad (25)$$

with bounds of 0 and 1000 m, where $H_0 = 40$ and 7 W m^{-2} for land and water, respectively, and $\Delta H = 40$ and 20 for land and water, respectively. For land, this results in d_{max} being approximately 1000 m for $H_{sfc} > 150$ W m^{-2} but can be less than 300 m (the minimum width required for activation) for H_{sfc} near 25 W m^{-2}. Over water, we use a more aggressive form, since the surface buoyancy fluxes are typically smaller, allowing d_{max} to vary from 300 to 1000 m between H_{sfc} of 0 and 70 W m^{-2}. We consider this regulation of d_{max} to be crude, but wide vertically coherent plumes are only found with strong forcing, so this at least helps limit excessively wide plumes in weakly-forced environments.

Each of these conditions are checked at every model timestep, dynamically regulating the maximum plume diameter d_{max} within each model grid column. The minimum d_{max} for all criteria is selected. Admittedly, there is some overlap between some of the criteria, but collectively, this effectively helps limit the use of excessively large plume sizes to only plausible conditions, maintaining a realism in the representation of the diverse set of vertically coherent plumes that may exist in a given atmospheric regime.

The turbulent mixing by the convective updrafts is also regulated by varying the fractional updraft area, a_u, over which the mean impact of the plume mixing is confined. This helps to further constrain the plume mixing in situations when plume mixing is questionable while unleashing the mixing in convincingly convective environments. The following controls regulate a_u:

1. Many EDMF schemes use a constant a_u, varying from 0.04 (Sušelj et al. 2013) to 0.05 (Kohler et al. 2011) to 0.1 (Soares et al. 2004; Neggers et al. 2009; Witek et al. 2011), or

one that can vary with height (Angevine et al. 2010). The MYNN-EDMF uses a constant a_u with height for each plume, but a_u is made to be a function of the surface buoyancy flux, H_{sfc}, to help act as a "soft triggering" mechanism. For this, we use a hyperbolic tangent function (Fig. 6):

$$a_u = a_{max}\left[\frac{1}{2}\tanh\left(\frac{H_{sfc}-H_0}{\Delta H}\right)+\frac{1}{2}\right], \quad (26)$$

where H_0 = 20 and 12 W m^{-2} for land and water, respectively, and ΔH = 50 and 30 W m^{-2} for land and water, respectively. For land, this results in a_u being approximately a_{max} (=0.1) for H_{sfc} > 150 W m^{-2} but can be as small as 0.03 for H_{sfc} near 0 W m^{-2}. Over water, we use a more aggressive form since the surface buoyancy fluxes are typically smaller. We consider this regulation of a_u to be crude but effective for imposing a soft trigger.

2. For tropical (and extratropical) cyclone-specific tuning, we assume that the fair-weather plume model has no validity in high-wind regimes. Therefore, we linearly taper down a_u to zero as the first model-layer wind speeds vary from 15 and 25 m s^{-1}.
3. Similar to the regulation of the maximum plume diameter d_{max}, we also apply a model grid-scale dependence to limit the impact of a_u at the high-resolution portion of the shallow-cumulus grey zone (600 m > Δx > 100 m). We use modified similarity functions from Honnert et al. (2011) and Shin and Hong (2013) to perform the tapering of a_u by applying a factor $P_{nonlocal}$ (Fig. 3, green curve). In accordance with the results of Angevine et al. (2020), this leverages the concept of effective resolution rather than grid resolution.

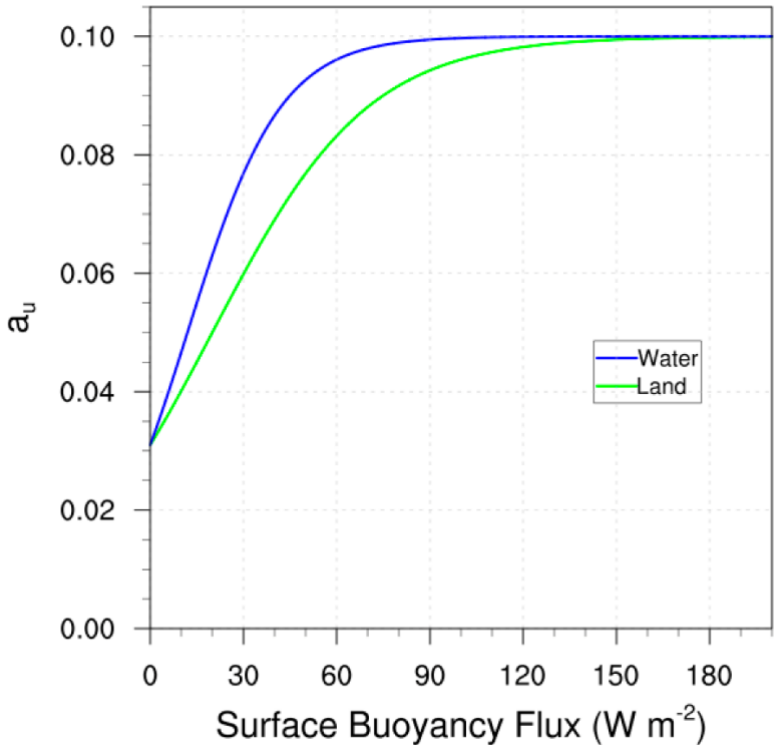

Figure 6. Functions to regulate the fractional updraft areal coverage, a_u, within a model grid column as a function of the surface buoyancy flux (H_{sfc}, W m^{-2}) described by Eq. (26) over water (blue) and land (green).

The minimum a_u determined by the three above conditions is used. The combined impact of these regulators of a_u as well as the natural tapering of the parameterized mixing appear to be first-order beneficial in regulating the nonlocal mixing within the grey zone, but testing below $\Delta x = 600$ m has been sparse.

The activation criteria of the mass-flux scheme in the MYNN-EDMF are threefold, where all three conditions must be met to activate:

1. The maximum plume size d_{max} (determined above) must be greater than the minimum plume size (300 m). Here, we assume that the eddy-diffusivity component can adequately represent the smallest plume mixing, whereas the mass-flux component focuses on the more energetic portion of the spectrum.
2. There must be a positive surface heat flux and the surface buoyancy flux must be greater than 5 W m^{-2}. This condition ensures that the mass-flux component is not actively transporting heat and moisture away from the first model level when the input forcing is too weak to realistically produce vertically coherent plumes.
3. The model surface layer must be superadiabatic with respect to θ_v in the lowest 50 m.

If any one of these conditions fail, then the mass-flux scheme will be inactive and the MYNN-EDMF is run in eddy-diffusivity configuration only for that model grid column at that specific timestep. Again, we admit to some overlap between the criteria, but a little redundancy does not substantially hinder performance computationally or skillwise.

Once the eight plume diameters and the total updraft area a_u is known, a_u must be divided appropriately among the eight plumes. That is, the turbulent transport contributed by each plume is mapped to a portion of a_u by way of the power law, which relates the number density, $\mathcal{N}$, of each plume size to the plume size following Neggers (2015):

$$\mathcal{N}(d) = Cd^x\,, \tag{27}$$

where d is the plume diameter, C is a constant of proportionality, and x is the power law exponent. This power law effectively weights the contributions of each of the various plumes to the total convective transport in the model grid column. With $x = -2$, each of the plumes covers an identical portion of a_u, but with $x > -2$, the largest plumes have a slightly larger contribution than the smallest plumes. We set $x = -1.9$ as in Neggers (2015), which is based off of a combination of observations and LES (Benner and Curry 1998, Neggers et al. 2003, Yuan 2011). C must be solved such that the total area of the eight plumes covers a_u (defined above), but since some plumes terminate at lower altitudes than others, the actual area covered by plumes drops below a_u and eventually to zero when all plumes terminate. This departs from Neggers (2015) in that we do not assume constant plume widths and updraft area, but the power law weighting is the same. Neggers (2015) planned to relax those assumptions in future research.

With the plume diameters, the total updraft area a_u, and the individual plume areas determined, the initialization and integration of the plumes can commence. Each of the updrafts are initialized at the top of the first model layer with vertical velocities:

$$w_{u_i} = p_w \sigma_w \tag{28}$$

where p_w varies from 0.1 to 0.4 between the smallest and largest plumes and σ_w is defined further below. The initialized w_u is not allowed to exceed 0.5 m s^{-1}. The initial plume properties for temperature and moisture are averages of the first and second model layers, representing a value at the interface between the first and second model layers. We assume that the averaged quantities are slightly boosted with a thermal and moisture excess defined as:

$$\theta_{li_{u_i}} = \theta_{li} + w_{u_i} C_{w\theta} \frac{\sigma_\theta}{\sigma_w}, \text{ and} \tag{29a}$$

$$q_{t_{u_i}} = q_t + w_{u_i} C_{w\theta} \frac{\sigma_{q_t}}{\sigma_w}. \tag{29b}$$

The constant $C_{w\theta} = 0.58$ from Sorbjan (1991) is used over land, which results in a negligible excess. This value is boosted by a factor of 16 over water, resulting in values near 0.1 K and 0.1 g kg^{-1} for temperature and moisture, respectively over the tropics in mean climatological conditions. The standard deviations of w, q_t and θ are specified as:

$$\sigma_w = C_\sigma w_* (z_s/z_i)^{1/3} (1 - 0.8 z_s/z_i) \tag{30a}$$

$$\sigma_{qt} = C_\sigma q_* (z_s/z_i)^{-1/3} \tag{30b}$$

$$\sigma_\theta = C_\sigma \theta_* (z_s/z_i)^{-1/3} \tag{30c}$$

where $C_\sigma = 1.34$, $z_s = 50$ m, w_* is the convective velocity, q_* is the surface moisture flux divided by w_* (kg kg^{-1}), and θ_* is the surface temperature flux divided by w_* (K). The above similarity expressions used to specify the excess heat and moisture were verified from observational studies over land (i.e., Wyngaard et al. 1971); for more details, see Cheinet (2003). We note that the excess quantities added to the parcel initializations only have a secondary impact on the evolution of the plumes. As found in other studies (Brast et al. 2016), the primary factors determining the fate of rising thermals are the entrainment rates and the background stability within the model grid column.

The MYNN-EDMF is designed to transport both momentum and TKE, but only momentum is transported by default. The namelist options, *bl_mynn_edmf_mom* and *bl_mynn_edmf_tke*, can be set to activate/deactivate the momentum and TKE transport, respectively (refer to section 9.3). When activated, the plume horizontal velocity components, u and v, are initialized by averaging u and v between the first and second model layers. We use the same averaging to initialize TKE. We do not add any additional excess quantities to these mean velocity components and TKE.

The vertical integration of each plume is performed with an entraining bulk plume model for the variables $\phi = \{\theta_{li}, q_t, u, v,$ and TKE$\}$. As in Teixeira and Siebesma (2000) and most other mass-flux schemes, we use a simple entraining rising parcel:

$$\frac{\partial \phi_{u_i}}{\partial z} = -\varepsilon_i (\phi_{u_i} - \phi) \tag{31}$$

where ε_i is the fractional entrainment rate, defined above, which regulates the lateral mixing of the updraft properties, ϕ_{ui}, with the surrounding air, ϕ.

The vertical velocity equation uses a modified version of that from Simpson and Wiggert (1969), with the buoyancy $B = g(\theta_{v,ui} - \theta_v)/\theta_v$ as a source term:

$$w_{u_i}\frac{\partial w_{u_i}}{\partial z} = -\varepsilon_i a w_{u_i}^2 - bB \qquad (32)$$

The coefficients a and b are discussed in several papers (e.g., Siebesma et al. 2003; de Roode et al. 2012). They represent the effect of pressure perturbations and subplume turbulence terms. The precise value of these coefficients is still a subject of research and diagnosed values from LES studies give different results in the cloud layer and in the subcloud layer. Based on some tuning for land-based shallow-cumulus simulations, we set $a = 2.0$. The impact of buoyancy is governed by b, which takes the value 0.15 when the buoyancy B is positive and 0.2 when B is negative, again selectively tuned for shallow-cumulus simulations. Some limits are in place to prevent unreasonably large values of w from developing, such as a maximum layer depth of $\Delta z = 250$ m used in Eq. (32) and a maximum updraft vertical velocity of $w_{ui} = 3$ m s^{-1} to curb this component's use to boundary-layer turbulence and shallow cumulus.

To summarize the plume integration procedure, at each model level, the following steps are performed for each of the eight plumes: (1) the entrainment rates are determined; (2) the plume variables are solved for using Eq. (31); (3) then the buoyancy term B and the vertical velocity (Eq. 32) are solved. This is repeated at each model level until each plume terminates by reaching a height at which w_{ui} becomes ≤ 0. Then, the mean convective mass-flux and plume properties are calculated by using the power-law weighting of each of the eight plumes.

Lastly, the linkage of the mass-flux transport to the creation of boundary-layer clouds is a primary incentive for adding the mass-flux component. As part of the integration process, at each model level, a saturation check is performed after calculating the plume thermodynamic state. If condensation occurs, latent heat is released, which directly impacts the parcel's buoyancy term in Eq. (32). This typically results in an acceleration of the parcel and an increased mass-flux M. For all condensed plumes, the determination of the cloud fraction and the contribution to the buoyancy production of TKE becomes an important additional step. We discuss this in section 4.

3.2 Downdrafts linked to cloud-top radiative cooling

In stratocumulus clouds, strong cloud-top cooling can make the upper cloud layer negatively buoyant, driving convective turbulence, even when the underlying surface fluxes are small (e.g., Deardorff 1980; Duynkerke and Driedonks 1987). In an attempt to incorporate this process into the MYNN-EDMF, a downdraft mass-flux component was developed as an upside-down reflection of the updraft model. The fundamental design is very similar and is only changed where necessary for the different application. The same spectral design is used, except only five downdrafts are used due to the smaller variation of sizes, spanning from 50 up to 500 m in diameter, which encompasses the mean sizes found in LES studies (Brient et al. 2019). In this first version, the maximum diameter, d_{max}, is constrained by two factors:

(1) the model's horizontal grid spacing Δx, specifically to be less than $1.2\Delta x$ (meters), which will not impact any mesoscale model configurations and only limit d_{max} in the lower end of the boundary layer grey zone, and
(2) the net radiative cooling at the cloud top:

$$d_{max} = \frac{\partial T}{\partial t_{rad}} f_d - 30\ , \tag{33}$$

where f_d is a negative tuning factor that also serves as a conversion factor from K s^{-1} to m (= -1.21×10^6 m s K^{-1}), which limits downdraft widths greater than 350 m to cooling rates greater than 28 K day^{-1}.

The constraints on d_{max} result in a variable increment width between each plume size, which will decrease as the maximum diameter decreases. If the maximum downdraft width falls below the minimum width (50 m), the downdraft component becomes inactive. More testing is required to ensure this scale- and forcing-adaptive behavior can truly represent turbulence associated with cloud-top radiative cooling in all model configurations.

Downdraft activation occurs where cloud fractions are > 50% and the radiative cooling rate exceeds 10 K day^{-1} at the top of the cloud. The relatively large threshold of 10 K day^{-1} may restrict activation to liquid clouds, which typically have larger cooling rates than ice clouds (Turner et al. 2018), so it may need to be relaxed if this downdraft component is to be fully extended to high-level clouds. The cloud fraction requirement may appear redundant, since low cloud fractions typically have small grid-mean cooling, but it is kept to ensure isolation to stratus clouds and to terminate downdrafts in cases where cloud fractions become small while cooling rates stay large, which may happen in very long radiation timesteps used in climate simulations. In theory, outside of the 10 K day^{-1} threshold for activation, the design of the downdraft component is general enough to be applied to any stratus cloud from fog to cirrus, but the current activation check only searches within a range of the k-level of the boundary layer height, k_{PBLH}, *i.e.*, between model grid levels from $MAX(k_{PBLH}-2,\ k=3)$ to $k_{PBLH}+20$. We neglect the lowest two model layers because the application of the nonlocal mass-flux model to a mixing between the lowest two adjacent layers is outside of its design; rather, we leave that to the eddy diffusivity component. The impacts of this downdraft model when applied to upper-level clouds are yet to be investigated.

Downdrafts are initialized at the model layer interface directly beneath the model layer where the radiative cooling and cloud fractions exceed the activation threshold. The initial downdraft properties for temperature and moisture are averages of two adjacent model layers representing the top of the cloud and the model level directly above it, along with a thermal and moisture deficit, respectively:

$$\theta_{li_{d_i}} = \theta_{li} + (i/5) C_{w\theta} \frac{\sigma_\theta}{\sigma_w}, \text{ and} \tag{34a}$$

$$q_{t_{d_i}} = q_t + (i/5) C_{wq}, \tag{34b}$$

where i is the downdraft index increasing with diameter width, $C_{w\theta} = -0.015$, $C_{wq} = MIN[-1/3 q_t,\ q_{sat}(T,p) - q_{sat}(T - C_{w\theta}\{\frac{\sigma_\theta}{\sigma_w}\},p)]$, so the deficits increase in magnitude as the downdraft width increase, reaching full magnitude only for the largest downdraft. Note that σ_w and σ_θ are defined differently from their updraft counterparts (Eqs. 30a and 30c):

$$\sigma_w = 0.3 w_{*rad}, \text{ and} \tag{34a}$$

$$\sigma_\theta = \theta_*. \tag{34b}$$

The radiationally-driven convective velocity, $w_{*\mathrm{rad}}$, and θ_* are calculated as:

$$w_{*rad} = 10\left[{}^{g}/_{\theta_{li_i}} \cdot \Delta z \cdot F_{rad}/(\rho \cdot c_p)\right], \tag{36a}$$

$$\theta_* = {}^{F_{rad}}\Big/_{\left(\rho c_p w_{*rad}\right)} - w_{ent}\,\frac{\Delta\theta_v}{\Delta z}_{ent}\Big/ w_{*rad} \tag{36b}$$

where g is the acceleration due to gravity, Δz is the depth of the model layer at the cloud top, ρ is the density, c_p is the specific heat of dry air at constant pressure, F_{rad} is the absolute value of the net radiative cooling at the cloud top (W m^{-2}), $\frac{\Delta\theta_v}{\Delta z}_{ent}$ is the gradient at the cloud top normalized to a 200 m depth in order to limit model grid configuration dependencies, and w_{ent} is the entrainment vertical velocity:

$$w_{ent} = \frac{1}{2}\frac{\theta_{sfc}}{g}\frac{w_{*rad}^3}{\Delta\theta_v}, \tag{37}$$

where $\Delta\theta_v$ is the difference in θ_v at the cloud top normalized to 200 m. The downdraft vertical velocities are initialized similarly to the updraft vertical velocities:

$$w_{d\,i} = p_w\sigma_w, \tag{38}$$

but for the downdrafts, p_w only varies from 0.1 to 0.3 between the smallest and largest downdrafts and σ_w is defined as in Eq. (34), not Eq. (30a). The range of the initialized w_d is constrained between −0.5 and 0 m s^{-1}, but is always negative. All other variables transported by the downdrafts are simply an average of the adjacent model layers, with no additional deficit/excess. However, for single-layer clouds, the subcloud properties are not used in the averaging. Instead, each variable transported is initialized with the values at the single cloud layer and, as before, the deficits are only added to the thermodynamic and moist variables.

The total fractional area of the downdrafts, a_d, is proportional to the magnitude of the net radiative cooling:

$$a_d = MIN(0.1 + 0.002F_{rad}, 0.3). \tag{39}$$

In contrast to the updrafts, the contribution of the individual downdrafts is not weighted to a_d by use of the power law, but instead are weighted equally, mostly because we do not know if the power law applies to radiatively-driven turbulence. Similar to the updrafts, there is a wind-speed dependence on a_d which linearly tapers it to zero between the lowest model-layer wind speeds of 10 and 25 m s^{-1}. This restricts the misuse of the vertically coherent downdraft model in high-shear environments, but this may need to be relaxed if the downdraft model is extended to upper-level clouds for which the near-surface winds may be irrelevant.

With the downdraft properties initialized, the integration of the downdrafts can begin. This is performed in the same manner as in the updraft counterpart, using Eqs. (31)–(32), except for integrating downward. The entrainment rate ε_i, is very similar to that used in the updrafts, but

modified to neglect the dependence upon the mean TKE in the boundary layer since some downdrafts may never penetrate below the stratified layer into the boundary layer:

$$\varepsilon_i = \frac{c_\varepsilon}{|w_{di}| d_i}, \tag{40}$$

where w_{di} is the downward vertical velocity (negative), so now needs the absolute value signs, and d_i is the diameter of each plume i. The parameter c_ε, which varied with ambient TKE for the updrafts, is now a constant set to 0.26. This diameter-dependent entrainment rate allows each downdraft to evolve differently; thus, attempting to represent a broad range of negatively buoyant downdrafts in stratus clouds.

After all downdrafts are integrated to their termination level where $w_{di} \geq 0$, the plume properties are known and are output to the *MYNN_TENDENCIES* subroutine for use in the tridiagonal solver (section 4) for nonlocal transport. The profiles of mass flux are used to calculate a TKE production term using Eq. (4) at all model levels below the cloud top. At the model interface immediately above the cloud top, there is an additional TKE source term, where w_{ent} [Eq. (37)] is used in Eq. (4) instead of the mass flux. This adds some weak vertical entrainment across the cloud-top interface, which typically has a small heating/drying impact below the cloud top. This TKE production term is sent to the *MYM_PREDICT* subroutine where the TKE is updated.

To summarize, after the initial downdraft properties are determined, the downdraft integration procedure begins. At each model level, the following steps are performed for each of the five downdrafts: (1) the entrainment rates are determined Eq. (40); (2) the plume variables are solved for using Eq. (31); (3) then the buoyancy term B and the vertical velocity Eq. (32) are solved. This is repeated at each model level until each downdraft terminates by reaching a height at which w_{di} becomes ≥ 0. Then the mean downdraft properties are calculated by using an equal weighting of each of the five downdrafts.

One major difference between the updraft and downdraft components is the latter does not create clouds, so it never creates latent warming. Instead, it only evaporates or sublimates clouds if the downdrafts penetrate the cloud base. As part of the integration process, at each model level, a saturation check is performed after calculating the plume thermodynamic state. If evaporation/sublimation occurs, the downdraft cools, which directly impacts the parcel's buoyancy term in Eq. (32). This typically results in an acceleration of the parcel and an increased downward mass flux M.

This relatively new downdraft component was added to the MYNN-EDMF but is not activated by default. This is primarily because it has not yet had sufficient testing in long-range forecasting, where its impacts are likely to be more pronounced. To activate this feature, an integer namelist parameter *bl_mynn_edmf_dd* must be set to 1.

3.3 Analytic profile of the buoyancy production of TKE

An alternative, and much simpler way, to incorporate the turbulence due to cloud-top radiative cooling into the TKE equation is to directly add a specified vertical profile of the buoyancy production/destruction term. The production/destruction term, which is part of Eq. (3):

$$P_b = 2\frac{g}{\theta_0}(\overline{w'\theta_v'}) \tag{41}$$

is modified, such that the heat flux, which was originally only a local buoyancy flux (explained further in section 4), includes a new nonlocal production component (last term on the right):

$$\overline{(w'\theta_v')} = -\beta_\theta\overline{(w'\theta_l')} - \beta_q\overline{(w'q_w')} - A\left(\frac{\theta_v}{g}\right)\frac{w_l^3}{h}(h-z)\left(1-\frac{h-z}{h}\right)^3 \tag{42}$$

where $A = 0.2(1 + a_2E)$ is the entrainment efficiency, taken from Nicholls and Turton (1986), except the value of a_2 is set to 8 following Wilson and Fovell (2018) and E is a function of the vertical gradients of θ_l and q_c. The convective velocity scale w_l is defined as,

$$w_l = \left[\frac{g}{\theta}\left(\overline{w'\theta'}\right)_{z_i} z_i\right]^{1/3} \tag{43}$$

but instead of using the heat flux at the surface, the heat flux associated with the radiative flux at the top of the cloud is used instead. The subscript and variable z_i correspond to the PBL height. The nonlocal nature of this new buoyancy production term is controlled by the linear-cubic vertical scaling function.

This feature was added to the MYNN-EDMF but never activated for use in an operational model. This is primarily because: (a) it lacks a specification of entrainment at the top of the PBL and (b) it may require further modification of the stability functions (section 2.3) to be more effective, because they can become very small in stable conditions, nullifying the impact of increased TKE production. By default, this feature is inactive. To activate this feature, an integer namelist parameter *bl_mynn_edmf_dd* must be set to 2. Note that this option will likely be removed in the future once the mass-flux downdraft code (*bl_mynn_edmf_dd* = 1) is deemed fully mature**.**

4. Solution of the EDMF Equations

We solve the equations for turbulent diffusion/transport simultaneously for eddy-diffusion and mass-fluxes using a semi-implicit method. The coding for this integration of the mass-flux scheme with the eddy-diffusivity tridiagonal solver was originally performed by Kay Sušelj (NASA-JPL). The discretization follows that which was proposed by Teixeira and Siebesma (2000) and Siebesma et al. (2007). For simplicity, this representation does not include a representation of density, which is required for scalar and momentum conservation, but density is included in the model code:

$$\frac{\phi^{t+\Delta t}-\phi^t}{\Delta t} = \frac{\partial}{\partial z}\left(K_\phi^t\frac{\partial\phi^{t+\Delta t}}{\partial z}\right) - \frac{\partial}{\partial z}[M_u^t(\phi_u^t-\phi^{t+\Delta t}) - M_d^t(\phi_d^t-\phi^{t+\Delta t})] + S_\phi^t \tag{44}$$

The generic variable ϕ on the r.h.s. is solved implicitly, but the ED and MF coefficients and the updraft fields are taken explicitly. S_ϕ is a source term, which can be surface-based or elevated. In the case of the mass-flux plume sources, plume properties at interface levels k+½ and k-½ are differenced to determine a source at center of layer k. All equations are solved on a staggered grid with the scalars and winds being defined on the middle of the model layers and the turbulence variables ($K_{H,M}$ and $M_{u,d}$) on model layer interfaces. Linear interpolation between levels is performed to transform TKE from mass levels to model interfaces to compute $K_{H,M}$. For the space discretization, standard second-order centered differences in space are used for the diffusion term and a simple first-order upwind scheme is used for the mass-flux integration. At the lowest model level, Eq. (41) is modified to include the surface fluxes, which are input from either a land-surface model or surface-layer scheme at water grid points. At the top of the atmosphere, the turbulent fluxes are set to zero. The tridiagonal matrix equation is solved by a downward elimination scan followed by back substitution in an upward scan (Press et al. 1992, pp. 42–43).

To safeguard against pathological behavior, the combined heat flux from all plumes between the first and second model levels is forced to be less than 75% of the upward surface heat flux. Enforcing this results in a modification of the total area of the updrafts throughout the depth of the penetrating plumes. This does not impose a strict limitation on the behavior of the mass-flux scheme, however, since this criterion is typically violated less than 2% of the time.

After the tendencies are calculated in the MYNN_TENDENCIES subroutine, there is a MOISTURE_CHECK subroutine that searches for negative mixing ratios of water vapor, cloud ice and cloud water. If any negative quantities are found, there is a procedure that borrows cloud mass from other model levels that have positive mixing ratio values until the negative values reach zero. When this adjustment from negative to zero mixing ratio occurs, some heat is added at that same level to conserve the total liquid potential temperature. No other checks for rain, snow, graupel, or hail are performed because they are not mixed within the MYNN-EDMF.

5. Subgrid Clouds and Buoyancy Flux

The representation of subgrid-scale (SGS) clouds and their connection to SGS turbulence is an important aspect in both general circulation and limited-area mesoscale models. This is typically accomplished by use of joint probability distribution functions, known as cloud probability distribution functions (cloud PDFs, also known as partial-condensation schemes), which can make use of either the higher-order moments or vertical gradients of the resolved-scale fields to determine the SGS cloud mixing ratio, cloud fraction, and the buoyancy flux. The more sophisticated forms (i.e., Golaz et al. 2002), which rely on additional prognostic equations, allow for a more direct physically consistent interaction between the higher-order turbulent quantities and the clouds, but come with an added computational cost. The simpler forms, such as Sommeria and Deardorff (1977), Mellor (1977), and Chaboureau and Bechtold (2002 and 2005; hereafter CB02 and CB05, respectively) are generally capable of representing first-order macrophysical aspects of subgrid clouds and are effective at reducing timestep variability in TKE-based schemes associated with grid-scale condensation. This is because the statistical representation of the SGS

cloud properties evolve more continuously and consistently as the background moisture changes in the model grid cell (Sommeria and Deardorff 1977).

The original MYNN was designed with a representation of SGS clouds using the cloud PDF from Sommeria and Deardorff (1977). In early versions of WRF–ARW (pre-v3.8), the macrophysical properties (SGS cloud fraction and SGS liquid water content) from this cloud PDF were only used to parameterize the SGS buoyancy flux; coupling to the radiation scheme was not yet performed. Since v3.8, more cloud PDFs have been integrated into the MYNN-EDMF with full coupling to the radiation. Namelist parameters were added to WRF–ARW to switch between different cloud PDFs (i.e., *bl_mynn_cloudpdf*) and to activate the coupling to the radiation scheme (i.e., *icloud_bl*; refer to section 8.3 for more details). We provide a description of each option for the namelist parameter *bl_mynn_cloudpdf* below. We describe *icloud_bl* and the coupling to the radiation scheme in section 6.1.

5.1 Stratus cloud PDF options

i. Original (Gaussian) form: *bl_mynn_cloudpdf* = 0

The original cloud PDF described in Nakanishi and Niino (2004) is based on the joint-Gaussian probability distribution functions for the liquid potential temperature θ_l and total water content q_t proposed by Sommeria and Deardorff (1977) and Mellor (1977). We essentially repeat their description here for comparison to alternative approaches later. In this approach, the standard deviation is estimated using the second-order moments in the MYNN. The cloud water content q_l can be written as:

$$q_l = 2\sigma_s \left[A_{cf} Q_1 + \frac{1}{\sqrt{2\pi}} exp\left(-\frac{Q_1^2}{2} \right) \right] \tag{45}$$

and the areal cloud fraction A_{cf} is:

$$A_{cf} = \frac{1}{2}\left[1 + erf\left(\frac{Q_1}{\sqrt{2}} \right) \right] \tag{46}$$

where *erf* refers to the error function. The normalized saturation deficit is:

$$Q_1 = \frac{a(q_t - q_{sat})}{2\sigma_s} \tag{47}$$

and the variance of the saturation deficit is:

$$\sigma_{s-strat}^2 = \frac{a^2}{4}(\langle q_t'^2 \rangle - 2b\langle \theta_l' q_t' \rangle + b^2 \langle \theta_l'^2 \rangle), \tag{48}$$

where the higher-order moments, q'^2, θ'^2, or $q'\theta'$, are either prognosed or diagnosed variables, depending on which closure level is used (see section 2.4), and a and b are thermodynamic functions arising from the linearization of the functions for the water vapor saturation mixing ratio:

$$a = \left(1 + \frac{L_v}{c_p}\delta Q_{sat}\right)^{-1}, \text{ and} \quad (49a)$$

$$b = \frac{T}{\theta}\delta Q_{sat}. \quad (49b)$$

$Q_{sl} \equiv Q_s(T_l)$ and $\delta Q_{sl} \equiv \partial Q_s/\partial T|$ are determined from the Tetens formula and the Clausius–Clapeyron equation, respectively, where Q_s is the saturation-specific humidity, $T_l = \theta_l T/\theta$, and L_v is the specific latent heat of vaporization.

ii. First-order form: *bl_mynn_cloudpdf* = 1,-1

When using the level 2.5 configuration of the MYNN, the higher-order moments except for the TKE are diagnostically calculated. Therefore, the higher-order moments may be less accurate, limiting their usefulness in the original cloud PDF. Motivated by this, we integrated an alternative form that avoids the use of the higher-order moments into the MYNN-EDMF. This form is based on Nakanishi and Niino (2004) and Kuwano-Yoshida et al. (2010). It uses a different expression for σ_s, based off of gradients of the first-order fields (θ_l and q_t),

$$\sigma_{s-strat} = \sqrt{\frac{a^2 l^2 B_2 S_H}{4}\left(\frac{\partial q_t}{\partial z} - b\frac{\partial \theta_l}{\partial z}\right)^2}, \quad (50)$$

but is also dependent upon on the mixing lengths, l, a closure constant B_2, the stability function for heat S_H, and thermodynamic variables a and b (defined above). Kuwano-Yoshida et al. (2010) added a lower limit on $S_H = 0.03$, arguing that a minimum is necessary for coarse vertical resolution model configurations to compensate for the under-resolved strength and variation of stratified layers. Therefore, this form is likely preferable to the original form for coarse-resolution modeling and possibly when run at level 2.5.

Note that the negative option (*bl_mynn_cloudpdf* = -1) is for testing only. This option disables the "nonconvective" portion of the SGS clouds so only the clouds from the convective (mass flux) are output and coupled to the radiation. This allows for a convenient way to test changes in the mass-flux scheme without the ambiguity of other sources of SGS clouds.

iii. Non-Gaussian form: *bl_mynn_cloudpdf* = 2,-2

In the past (pre-2023), this option used a modified form of CB02 and CB05. Over time, it has evolved to an extent that it now barely resembles its ancestor. It is still classifiable as a statistical SGS cloud scheme for representing nonconvective (or stratus) clouds in that the cloud fraction and diagnosed cloud water are functionally dependent on a single variable, the normalized mean saturation deficit Q_l, making the diagnosed cloud fraction and cloud water amounts directly linked to the simulated turbulence. The subgrid variability of the saturation deficit, $\sigma_{s\text{-}strat}$, is based off of the higher-order moments, similar to option 1 (Eq. 48):

$$\sigma_{s-strat} = (\langle q_t'^2\rangle - 2b\langle\theta_l' q_t'\rangle + b^2\langle\theta_l'^2\rangle)^{1/2}, \quad (51)$$

where b is defined in Eq. (49b). One major difference found in this updated cloud PDF is all three terms on the r.h.s. of Eq. (51) are only used when using the level 3.0 configuration (discussed in

section 2.4) when all of the higher-order moments (q'^2, θ'^2, and $q'\theta'$) are prognosed (and generally more reliable). When configured to run at level 2.7, only the first and third terms are used, whereas only the first term is used at level 2.5 and 2.6, which is capable of representing the majority of the subgrid cloud variability in most cases. This allows for the most reliable estimate of $\sigma_{\text{s-strat}}$ possible for each closure option.

We have added improved constraints, linking lower bounds of $\sigma_{\text{s-strat}}$ to a small fraction of the grid-mean total water, which keeps the estimates realistic in cases when the simulated turbulence becomes questionable. This can especially help the level 2.5 configuration, where none of the three additional higher-order moments are prognosed.

Then the normalized saturation deficit is calculated as:

$$Q_1 = \frac{q_t - q_{sat}}{\sigma_s}, \tag{52}$$

There is an effective but questionable constraint added to ensure a cloud fraction is assigned for model grid cells that have a nonzero cloud water (or ice) mixing ratio from the microphysics scheme while being well undersaturated. This can be caused by cloud water or ice that either settle into unsaturated model layers from above and/or the advection (or other model numerics) that diffuse cloud species into adjacent unsaturated layers. In this case, the background moisture and turbulence are too low, so the diagnosed $\sigma_{\text{s-strat}}$ may not be sufficient to produce a nonzero cloud fraction, A_{cf}. A patch was suggested by Greg Thompson (personal communication) to use an extension roughly following Xu and Randall (1996), where the estimated *RH* is increased and then mapped to an increased Q_1:

$$RH_{adj} = RH_{crit} + R_1[R_2 + \log(q_x)], \text{ and} \tag{53a}$$
$$Q_{1-adj} = -3 + 3[(RH_{adj} - RH_{crit})/(1 - RH_{crit})], \tag{53b}$$

where RH_{crit} = 0.83; R_1 and R_2 are 0.037 and 10.0, respectively, when $q_x = q_i + q_s$; and R_1 and R_2 are 0.065 and 5.0, respectively, when $q_x = q_l$. The maximum of Q_1 and $Q_{1\text{-adj}}$ is used for the cloud fraction specification (below). This may currently be tuned to work specifically for the Thompson or TEMPO aerosol-aware microphysics schemes, which tend to have less cloud cover than most other commonly used schemes. If other microphysics schemes are used and excessive cloud optical depth is found, Eq. (53b) could simply be set equal to the value calculated by Eq. (52) to disable the patch.

The cloud fraction, A_{cf}, has been changed to use two different versions of the same functional form for below and above the PBL height:

$$A_{cf} = max\left\{0, min\left[1, \frac{1}{2} + C_1 \text{atan}\left(C_2\{Q_1 + C_3\}\right)\right]\right\}, \tag{54}$$

where C_1 = 0.35, C_2 = 3.6, and C_3 = 0.05 below the PBLH height and C_1 = 0.39, C_2 = 1.6, and C_3 = 0.55 above the PBLH height. The two forms are blended across the PBL height linearly between ± 150 meters. The less aggressive form below the PBL height helps reduce excessive cloud cover in the PBL, especially over water.

Note that in most modeling frameworks, A_{cf} is output in the *CLDFRA_BL* array, and the subgrid-scale q_c and q_i (determined below) are output in the *QC_BL* and *QI_BL* arrays, respectively. These arrays are then used by other model components (section 6.1).

The hydrometeors are then specified as:

$$q_x = MIN\left(\sigma_{s-strat}, 0.025 q_t A_{cf}\right), \tag{55}$$

which is then separated into liquid and cloud by a temperature-dependent function:

$$Frac_{liq} = MIN[1, MAX\left(0, \{T - T_{ice}\}/\{T_{liq} - T_{ice}\}\right)], \tag{56}$$

where T_{ice} = 235 K and T_{liq} = 268 K.

As noted above, we use the negative option (*bl_mynn_cloudpdf* = -2) for testing purposes only. This option disables the "nonconvective" portion of the SGS clouds so simulations can be performed with only the convective SGS clouds (from the mass-flux scheme). This allows for a convenient way to isolate testing to the mass-flux clouds without the ambiguity of other sources of SGS clouds.

5.2 Subgrid clouds from the updraft mass-flux component

The standard deviation of the subgrid saturation deficit, $\sigma_{\text{s-conv}}$, is proportional to the mass flux, M, and the vertical gradient of the total water:

$$\sigma_{s-conv} = \alpha_{conv} \tau_c M \frac{\Delta q_t}{\Delta z}, \tag{57}$$

where α_{conv} is a constant of proportionality (≈ 5) and τ_c is timescale on the order of the eddy-turnover timescale (≈ 1800 s). A practical lower bound for σ_{s-conv} is a relationship from Stefan de Roode (personal communication) that was tested for use in place of Eq. (56) but resulted in a lack of variation in cloud fraction for distinct shallow-cumulus regimes. For this reason, it could not be the primary form adopted; however, it was determined that it would still make for an excellent physically based lower bound:

$$\sigma_{s-conv-min} = 3 a_u (q_{t-up} - \overline{q_t}), \tag{58}$$

where $q_{t\text{-}up}$ is the total water in the updraft at a given model level and $\overline{q_t}$ is the grid-mean total water. Eq. (58) can make a small impact in very thin/sparse shallow cumulus regimes but does not play a role in any shallow-cumulus environments with moderate to large (15–50%) cloud cover.

The calculation of the convective cloud fraction, $A_{cf\text{-}conv}$, is similar to the stratiform counterpart where the normalized saturation deficit, Q_1, is calculated as in Eq. (52) and then $A_{cf\text{-}conv}$ is calculated using Eq. (54) except with C_1 = 0.36, C_2 = 1.8, and C_3 = 0.2. A lower bound of $A_{cf\text{-}conv}$

is set proportional to the updraft area, a_u, using a proportionality factor of 1.2 over water and 1.8 over land. These values were determined using LES but the work was not published.

The calculation of *suspended* grid-mean cloud mixing ratio from the updraft component, $q_{c\text{-}conv}$, leverages the instantaneous cloud water that is fluxed upwards and condensed in the updrafts, $q_{c\text{-}up}$, multiplied by a proportionality factor and the updraft area, a_u:

$$q_{c-conv} = 1.2 q_{c-up} a_u. \tag{59}$$

In most cases, only the largest plumes penetrate above the lifting condensation level and produce clouds. The thinner plumes that cannot penetrate high enough do not contribute to a_u above their termination height. This simple diagnostic Eq. (59) helps improve estimates of the total suspended cloud water that may linger over multiple timesteps if the subgrid clouds are allowed to evolve in a budgeted sense. Work is ongoing to prognose the subgrid-scale cloud water but this is still under development.

In cases where there are both subgrid stratus (estimated in section 5.1) and convective clouds, they are blended in a way that prioritizes the estimates from the mass-flux scheme. The maximum of the cloud fractions is used, i.e., $A_{cf} = MAX(A_{cf\text{-}strat}, A_{cf\text{-}conv})$ because they are independent estimates of the subgrid-scale clouds at the same grid point. Then the blended mixing ratios are calculated using a weighting function, w_{mf}:

$$w_{mf} = A_{cf-conv} / MAX(A_{cf-conv}, A_{cf-strat}), \text{ and} \tag{60a}$$
$$q_c = q_{c-conv} w_{mf} + q_{c-strat}(1 - w_{mf}). \tag{60b}$$

As noted in the previous section, in most modeling frameworks, A_{cf} is output in the *CLDFRA_BL* array and the subgrid-scale q_c and q_i are output in the *QC_BL* and *QI_BL* arrays, respectively. These arrays are then used by other model components (section 6.1).

5.3 Estimating effective static stability

Estimating the effective static stability (ESS) is an essential aspect of any moist-turbulence parameterization, which must take into account the differences in dry and moist parcel ascent as well as the local and nonlocal nature of turbulent mixing within the environment. Conversely, an accurate estimation of turbulence and subgrid-scale clouds within a model grid cell can improve an estimate of the ESS, which plays an important role in determining the buoyancy production/destruction, vertical transport, and dissipation of TKE. This two-way dependence makes the estimation of ESS very important. The ESS can directly impact all three components of the eddy diffusivity/viscosity (TKE, mixing length, and stability functions), resulting in a powerful influence on the overall turbulent mixing in partially condensed grid cells.

There are several approaches to account for the effects of latent heat release in modifying the static stability, but there are currently only two options of ESS estimations in the MYNN-EDMF: the original approach, which uses the so-called buoyancy-flux equations derived by Sommeria and Deardorff (1977) and Mellor (1977), and a second approach, which is a modified form of O'Gorman (2011). This option is now selectable with the namelist parameter *bl_mynn_ess*.

i. Original buoyancy-flux form: *bl_mynn_ess* = 0:

This method converts the vertical gradient of θ_{li} to a gradient of *effective* θ_v by use of the buoyancy-flux functions, Eqs. (62a,b), which makes use of the estimated cloud fraction and turbulence through either the higher-order moments or first-order gradients, depending on the selected option for *bl_mynn_cloudpdf*. Within partially or fully condensed grid cells, the conversion is only approximate because the vertical gradient conversion will be destabilized.

The form of the buoyancy flux, $w'\theta_v'$, in the MYNN TKE equation is:

$$\langle w'\theta_v' \rangle = \beta_\theta \langle w'\theta_l' \rangle + \beta_q \langle w'\theta q_t' \rangle \tag{61}$$

where the buoyancy flux functions are:

$$\beta_\theta = 1 + 0.61q_t - 1.61q_l - Rabc \text{ , and} \tag{62a}$$
$$\beta_q = 0.61\theta + Rac. \tag{62b}$$

The functional relationships for *a* and *b* are given by Eqs. (49a) and (49b), respectively, and:

$$R = A_{cf} - \frac{q_l}{2\sigma_s}\frac{1}{\sqrt{2\pi}}\exp\left(-\frac{Q_1^2}{2}\right),$$
$$c = (1 + 0.61q_t - 1.61q_l)\frac{\theta}{T}\frac{L_v}{c_p} - 1.61\theta \ .$$

The buoyancy flux functions (Eqs. 62a,b) are also used to estimate the ESS using the subgrid cloud property estimates:

$$\theta_{v-eff} = \beta_\theta \theta_{li} + \beta_q q_t. \tag{63}$$

This *effective* θ_v is then used in the calculation of the Brunt-Väisälä frequency and the Richardson number, which both play a central role in regulating the behavior of the MYNN-EDMF.

ii. Modified O'Gorman (2011) form: *bl_mynn_ess* = 1 (default):

This approach destabilizes the lapse rate in grid cells with both turbulence (local turbulence or nonlocal mass-flux transport) and clouds by adding a negative adjustment proportional to the vertical gradient of the saturated equivalent potential temperature (θ_{es}), the parameterized turbulence (TKE and *M*), and cloud fraction (A_{cf}):

$$\left(\frac{\partial \theta_v}{\partial z}\right)_{eff} = \frac{\partial \theta_{li}}{\partial z} + \lambda \frac{\partial \theta_{es}}{\partial z}, \tag{64}$$

where the second term on the r.h.s. is constrained to be nonpositive and the variable $\lambda = C_\lambda \cdot max(0.5 \cdot TKE^{-2}, M) \cdot A_{cf}$. The coefficient C_λ has units of s m^{-1} (i.e., eddy timescale / PBL depth

~ 1.8). In the code, C_λ is adjustable for different environments (land PBL, marine PBL, and free troposphere). Also, some marine cyclone-awareness has been added, which tapers C_λ to zero at high wind speeds within the marine PBL.

By using the saturated equivalent potential temperature, θ_{es}, which generally has a more negative lapse rate in the tropics (especially below 700 hPa), this algorithm is most impactful in destabilizing partially saturated layers in the tropics compared to the mid-latitudes and even less so at the poles (O'Gorman 2011). The biggest departure from O'Gorman (2011) is the variable λ, which was changed to better fit the design of the MYNN-EDMF.

6. Communication with Other Model Components

6.1 Radiation Scheme

The SGS clouds produced by the MYNN-EDMF (section 5) are coupled to the longwave and shortwave radiation schemes when certain model-dependent namelist settings are enabled. For WRF and CCPP, the parameter *icloud_bl* is set to 1, while in MPAS, the namelist flag *config_radt_cld_scheme* is set to "cld_fraction_mynn". When these settings are active, the SGS cloud fraction, *CLDFRA_BL*, and the SGS cloud mixing ratios for water and ice, *QC_BL and QI_BL*, respectively, are added in a complementary manner to the resolved microphysics species only within the radiation driver. The following two steps are performed:

(1) The cloud fraction from the MYNN-EDMF is used as the primary cloud fractions, but additional subgrid cloud fractions and cloud water content can be added from a deep-convection scheme if the convection scheme is active and it provides such output.

(2) If the resolved-scale cloud liquid and cloud ice (from the microphysics scheme), q_c and q_i, is less than 10^{-6} kg kg^{-1} and 10^{-8} kg kg^{-1}, respectively, and there exists a nonzero SGS cloud fraction, then the SGS components (*QC_BL and QI_BL*) are added to their respective resolved-scale components.

The *QC_BL* and *QI_BL* from the MYNN-EDMF are output as grid-mean values, so they can be directly added without the need to multiply by the cloud fraction. The updated q_c, q_i, and *CLDFRA* are then used as input into the radiation schemes.

An additional step needed for the radiation scheme is the specification of the effective radii for each subgrid cloud species. In most model frameworks, if not specified, constant values are likely assigned for each species, but this is quite crude. Some modeling frameworks have a method to estimate a number concentration for the subgrid cloud species and then the effective radii can be estimated from the mixing ratios and number concentrations. In CCPP, a linear temperature-dependent specification of the effective radii for ice in nonconvectively-induced cirrus following Mishra et al. (2014, their Fig. 6b):

$$r_{e\_ice} = a_{re} + b_{re}T, \tag{65}$$

where a_{re} = 173.46, b_{re} = 2.14, and T is in Celsius.

After exiting the radiation schemes, the original values of q_c and q_i are restored, so the SGS clouds do not impact the resolved-scale moisture budget. Ongoing development is happening to combine the MYNN-EDMF subgrid clouds seamlessly with the resolved-scale clouds (section 9) to obtain a prognosed unified budget with perfectly consistent thermodynamics and precipitation processes, but this work is not yet complete.

6.2 Surface-Layer and Land-Surface Model

In all model frameworks of which the authors are aware, the MYNN surface-layer scheme (Olson et al. 2021) is called prior to the call to the land-surface model (LSM), which is called prior to the PBL schemes (i.e., the call order is MYNN surface-layer scheme, then LSM, then MYNN-EDMF). The MYNN surface-layer scheme computes the surface stability parameter *z/L* (which is later recomputed inside the MYNN-EDMF), surface scalar transfer coefficients, and the momentum and scalar fluxes (u_*, *HFX*, and *QFX*) over land, water, and snow grid points; however, the LSM recalculates the scalar fluxes over land and snow grid points. One exception is the Noah-MP LSM, which ignores the input transfer coefficients and recalculates everything over land. In that case, Noah-MP uses its own internal surface-layer scheme over land, but the model configuration will still require the use of a surface-layer scheme for water grid points.

The MYNN-EDMF needs the following surface-related inputs: u_*, *HFX*, and *QFX*. These three variables are used for a variety of calculations, such as lower-boundary conditions for the solver or initializing the parcels for the mass-flux scheme. The internally recomputed surface stability parameter *z/L* is used for computing the surface-layer length scale and the lower-boundary condition for TKE.

6.3 Microphysics Scheme (Thompson and TEMPO-centric)

Different modeling frameworks sometimes split state variables into packaged arrays or derived-data type arrays. For example, WRF–ARW splits the moisture species into a defined set of "moist" and "scalar" arrays, but this is not universal across all modeling frameworks. Thus, while the MYNN-EDMF submodule can no longer be designed to simply mix a generic set of microphysics variables, in most cases it will do so anyway. The MYNN-EDMF scheme, as it currently exists in submodule form, uses five namelist variables to control the mixing of microphysical variables (Table 2).

The option most relevant to any microphysics scheme is *bl_mynn_cloudmix*; when set to 1 (default, recommended), the MYNN-EDMF provides tendencies for q_c, q_i, q_{nc} and q_{nc} (the latter two also require *bl_mynn_mixnumcon* = 1, see below). Other variables, such as graupel q_g, snow q_s, hail q_h, and rain q_r are not mixed due to numerical instabilities found when mixing hydrometeors with relatively large deposition velocities (though note that not all microphysics schemes were impacted by the mixing of these species). For each variable, checks are in place to make sure the variable exists, with the additional control options in Table 2 existing for testing or scheme compatibility.

Table 2. The cloud- and aerosol- specific namelist options from the full namelist (Table 4) are reproduced here for the discussion on coupling to microphysics. The namelist options, values, and description are given in columns 1, 2, and 3, respectively.

Namelist Option	Value	Description and Default Configuration
bl_mynn_cloudmix	0	Deactivate the mixing of any water species mixing ratios
	1	Activate the mixing of all water species mixing ratios (default)
bl_mynn_mixqt	0	Mix individual water species separately (default)
	1	Does not work for complex (more than warm rain) microphysics schemes, keep set to 0
bl_mynn_mixnumcon	0	Deactivate the mixing of number concentrations (default)
	1	Activate the mixing of number concentrations for cloud water and ice
bl_mynn_mixaerosols	0	Deactivate the mixing of Thompson/TEMPO aerosols
	1	Activate the mixing of Thompson/TEMPO aerosols (default)
bl_mynn_mixscalars	0	Deactivate mixing of generic scalar array (default)
	1	Mix generic scalar array (need to set up manually in driver)

If *bl_mynn_mixnumcon* = 1, MYNN-EDMF provides tendencies for q_{nc} and q_{ni}, but does not mix any other number concentrations (i.e., q_{ng}, q_{ns}, $q_{nh,}$ etc) that may exist. This additional control for q_{nc} and q_{ni} was added for two reasons: (1) the mixing of number concentrations appears to have a secondary impact in most cases, and (2) the Thompson-Eidhammer MicroPhysics scheme for Operations (TEMPO) has a machine-learning specification of the number concentrations to replace the need to prognose and advect them at each timestep. Because of this, the default value of *bl_mynn_mixnumcon* is (or is planned to be) set to 0. If *bl_mynn_mixnumcon* is configured to 1, then liberal lower limits are set for q_{nc} and q_{ni} before and after mixing. This was done because negative incoming values were discovered in certain modeling frameworks and the negative values would spread if lower limits are not enforced. The magnitude of the lower limits (q_{nc_min} = 1000 and q_{ni_min} = $1.0\text{x}10^{-6}$ kg^{-1}) are set to be small enough to have little or no impact on the cloud or rain forecasts when tested with TEMPO.

The mixing of Thompson/TEMPO water- and ice-friendly aerosols, *qnwfa* and *qnifa*, as well as black organic carbon, *qnbca*, is active when *bl_mynn_mixaerosols* is set to 1 (default). No lower bounds are set before or after mixing in MPAS because the surface aerosol fluxes have been tuned to be reasonable. Upper and lower bounds are applied in WRF-ARW because the budget is not well constrained. Currently there is no consideration of the aerosol effects on the SGS clouds in the MYNN-EDMF.

If additional scalars are to be mixed (other than q_c, q_i, q_v, q_{nc}, q_{ni}, *qnwfa*, *qnifa*, *qnbca*, and θ_{li}), they can be added to a generic *scalars* array in the driver and the namelist parameter *bl_mynn_mixscalars* can then be set to 1 (default = 0). This will allow any number of additional scalars to be mixed both locally and nonlocally within the MYNN-EDMF. Alternatively, in WRF-ARW, there is an additional subroutine *mix4d* located in the PBL driver, which makes use of the eddy diffusivity from the MYNN-EDMF to locally mix a generic set of scalars when the namelist parameter *scalar_pblmix* is = 1. We advise not using this alternative approach because it will not mix the scalars nonlocally. If no scalars are added to the scalar array in the MYNN-EDMF driver then keep *bl_mynn_mixscalars* to 0, since it will only wastefully mix zeros.

6.4 Fog Settling

The original MYNN included a simplified (full-column) gravitational settling of cloud droplets as described in Nakanishi (2000), which used the formulation of the cloud droplet deposition velocity proposed by Duynkerke (1991). In older versions of WRF–ARW (pre-v3.7), this physical process was only represented in the MYNN PBL scheme. The namelist parameter, *grav_settling* (inactive by default, = 0)*,* activates this physical process when set to 1. In more recent versions of WRF–ARW, as well as in all MYNN-EDMF implementations in MPAS v8.2+ and CCPP, this process has been removed from the MYNN-EDMF and now only exists in WRF-ARW, where it was moved into a separate module (phys/module_bl_fogdes.F) called within the PBL driver. This allows gravitational/fog settling to be used in combination with any PBL scheme. As part of this fog deposition module, a vegetation-dependent deposition velocity based on Katata et al. (2008) was added to impact the deposition velocity in the lowest model level in advective situations. Note that *grav_settling* should be set to zero (kept inactive) when using the Thompson, TEMPO, or any other microphysics scheme that already includes the representation of cloud droplet settling. Consult with your local microphysicist to see if this process is already included in your microphysics scheme of choice.

Note that in WRF-ARW, when *grav_settling* = 1 (activated), the tendency for q_c, calculated in phys/module_bl_fogdes.F, and is added to the PBL tendency array *RQCBLTEN*. Thus, an analysis of moisture tendencies from the MYNN-EDMF (or any other scheme) should only be undertaken with *grav_settling* = 0, to isolate the contribution from the boundary layer schemes.

6.5 Orographic Drag

The MYNN-EDMF is not dependent upon any fields from the orographic drag scheme in WRF–ARW, MPAS, or CCPP; however, some drag schemes need *KPBL* and/or *PBLH* as input, which are both calculated in the MYNN-EDMF as described in section 7.1 (or by other PBL schemes). In some model frameworks, like WRF-ARW and MPAS, the tendencies from the orographic drag scheme are added to PBL-tendency arrays *RUBLTEN*, *RVBLTEN,* and *RTHBLTEN*, which are later used to update the state variables. Thus, in order to analyze the momentum tendencies from the MYNN-EDMF (or any other PBL scheme) in isolation from the orographic drag tendencies, do not activate an orographic drag scheme (in WRF-ARW, set *gwd_opt* = 0 in the dynamics section of namelist.input). The intertwining of the boundary-layer and orographic drag tendencies should be considered a questionable configuration if not a bug, but some model code managers may require considerable coaxing to separate these tendencies.

6.6 Dust and Smoke

The mixing and nonlocal transport of smoke and dust has been integrated into the MYNN-EDMF for components of operational applications, such as HRRR-Smoke (Ahmadov et al. 2017; Li et al. 2025). This application leverages a generic “chem” mixing subroutine, *MYNN_MIX_CHEM*, which will mix all chemical species both locally and nonlocally. Within this subroutine, an additional feature can be activated when the input control flag (which currently only exists in the community CCPP release), *enh_mix*, is set to true. In this case, the eddy diffusivity, K_H, is increased over grid cells where the input estimates of fire radiative power, *FRP*, are nonzero. This

only impacts the local diffusion; the nonlocal transport by the mass-flux component is not yet modified, but it will still perform nonlocal transport of the dust and smoke.

6.7 Wind Farm Parameterization

There are several types of wind farm parameterizations (WFP), and the couplings of them to various turbulence parameterizations is not known to the first author, but the MYNN-EDMF has been coupled in WRF-ARW with the Fitch WFP scheme (Fitch et al. 2013) for over a decade. This scheme estimates a drag on the winds at model layers that intersect the defined turbine-rotor layer while also adding a source of TKE due to turbine mixing. The TKE source is directly added to the *QKE* variable within the Fitch WFP scheme, whereas the momentum tendencies are added to the *u*- and *v*- PBL tendency arrays. No additional information is necessary to pass into the MYNN-EDMF for proper coupling, but the user must again take notice that part of the momentum tendencies from the "PBL" are not computed by the boundary layer scheme in this configuration and the TKE budget output from the MYNN-EDMF will be missing the contributions from the Fitch WFP scheme.

6.8 Stochastic Parameter Perturbations

Stochastic parameter perturbation (SPP) is implemented in the MYNN-EDMF by modifying select physical parameters or variables with perturbation patterns that evolve according to chosen decorrelation time and/or length scales (Jankov et al. 2017; Jankov et al. 2019; Kalina et al. 2021). Each perturbed parameter or variable was chosen because it had both some degree of uncertainty and sensitivity that could help produce spread in an ensemble system when uniquely perturbed in each ensemble member. The best example and details of the implementation of SPP into the MYNN-EDMF can be found in Kalina et al. (2021) for an experimental WRF-based ensemble configuration.

Although the SPP code is available for use in the MYNN-EDMF, the implementation of a random pattern generator is required in each model framework to produce spatially and temporally varying perturbation fields that are passed into the MYNN-EDMF (and other SPP-capable physical parameterizations). Currently, only WRF and CCPP have been developed with SPP capability; this capability is under development for MPAS. Table 3 summarizes the parameters and variables perturbed in the MYNN-EDMF.

Table 3. List of stochastically perturbed fields and information on how each field was perturbed spatially, temporally, and in magnitude.

Field	Field type	Spatial decorrelation length scale	Temporal scale	Percent magnitude of perturbation (for one standard deviation)
K_H *and* K_M	Diagnostic	150 km	6 hrs	30%
Background q_v	Diagnostic	150 km	6 hrs	10%
Entrainment rate	Diagnostic	150 km	6 hrs	10%

7. Description of Output Fields

7.1 Hybrid Diagnostic Boundary-Layer Height (PBLH)

Some of the content discussed in this memorandum requires the MYNN-EDMF to use the PBL height, z_i, as an internal variable, so we must give extra care for an accurate diagnostic for z_i. Results from Lemone et al. (2013, 2014) show that a potential temperature-based definition of z_i is generally reliable for convective boundary layers, whereas TKE-based definitions perform well for stable boundary layers. Steeneveld et al. (2007) compared stable PBL height diagnostics within stable conditions and surprisingly found the simple u_*-dependent form from Koracin and Berkowicz (1988) to perform best. Therefore, we implemented a hybrid definition, which uses the potential temperature-based definition in convective boundary layers while offering a choice of the TKE-based or u_*-based definitions for the stable boundary layer.

For the convective PBL, we use a virtual potential temperature-based version of the boundary layer height definition, $z_{i\theta}$, of Nielsen-Gammon et al. (2008). This algorithm first searches the lowest 200 m of the atmosphere to find the height of the minimum virtual potential temperature (θ_{v_min}). This helps to reduce the impact of surface-based superadiabatic layers on the diagnosis of $z_{i\theta}$. Then $z_{i\theta}$ is determined to be the height at which $\theta_v = \theta_{v\_min} + \Delta\theta_v$, where $\Delta\theta_v$ is set to 0.75 K over water and 1.25 K over land.

For the stable PBL, there is an internal parameter, *stable_method*, within the subroutine *GET_PBLH*, which allows the selection of the TKE-based definition (*stable_method* = 0) or the or u_*-based definition (*stable_method* = 1, default):

- The TKE-based diagnostic (z_{iTKE}) is the height at which the TKE at the surface, $\mathrm{TKE_{sfc}}$, decreases below a threshold value, $\mathrm{TKE_{min}}$. We chose the quantity $\mathrm{TKE_{min}}$ to be 5% of the $\mathrm{TKE_{sfc}}$ —a criterion chosen independently by Kosović and Curry (2000) and used in Cuxart et al. (2006). $\mathrm{TKE_{min}}$ is also bound to be greater than 0.01 $\mathrm{m^2\ s^{-2}}$ in the case of stagnant cold pools, where the lack of a lower limit can result in an excessively large estimate of z_{iTKE}. This method performs reasonably well but can result in visible discontinuities arising from the imperfect determination of $\mathrm{TKE_{min}}$. To prevent catastrophic irregularities, z_{iTKE} is bound to be within ± 300 m from $z_{i\theta}$.
- The u_*-based diagnostic (z_{iu*}) was implemented as a simple alternative to the z_{iTKE} diagnostic, which can remove some of the inherent regularities of the z_{iTKE} diagnostic, but its use must be isolated to stable conditions. The original form from Koracin and Berkowicz (1988) is a simple one-line calculation: $z_{iu*} = 700u_*$. We found that in very stable conditions, the resulting estimates of z_i may be slightly high biased, which may not be a fault of the diagnostic but rather a sensitivity to the calculation of u_* and related biases in the modeling system. Until a more thorough investigation of u_* can be performed, this diagnostic is implemented in a way that allows for a variable proportionality parameter, varying from 400 to 700 as $z_{i\theta}$ varies between 0 and 200 m.

Then the two definitions are blended such that $z_{i\theta}$ will dominate for neutral and unstable conditions (when $z_{i\theta} > 200$ m), while z_{iTKE} or z_{iu*} will dominate for stable conditions ($z_{i\theta} < 200$ m), with $z_{i\theta}$ used as an indicator of stability to facilitate the blending. We use a hyperbolic tangent for blending the two definitions, similar to Eq. (10b), but replace z_i with $z_{i\theta}$, set Δz to 200 m, and set the blending

depth determined by the denominator in the hyperbolic tangent argument to 170 m. This hybrid algorithm has been shown to accurately diagnose the boundary-layer height throughout a diurnal cycle (Fitch et al. 2013).

7.2 Initialized Plume Excess (EXCESS_H, EXCESS_Q)

The surface-based convective plumes are initialized according to Eqns. (25) and (26), resulting in small boosted values of heat (*EXCESS_H*) and moisture (*EXCESS_Q*), respectively. The units are K for *EXCESS_H* and kg kg^{-1} for *EXCESS_Q*. These excess values are now available as output from the MYNN-EDMF but may not be output by default in every modeling framework.

7.3 Maximum Mass Flux (MAXMF)

MAXMF is a two-dimensional diagnostic output from the mass-flux scheme with units of m s^{-1}. We calculate this field by searching for the maximum mass flux at levels for all plumes active in a particular model grid column. There is no level information kept to describe the height at which the maximum mass flux occurred. However, to provide information on whether any of the plumes in a grid column had condensed or not, we keep the maximum mass flux positive if any plume reaches the lifting condensation level and produces a shallow-cumulus cloud. We multiply the maximum mass flux by −1 if no plumes condense, since it is only a diagnostic output and does not impact the functionality of the scheme.

7.4 Maximum Width of Active Plumes (MAXWIDTH)

MAXWIDTH is a two-dimensional field which shows the maximum plume size represented by the spectral updraft mass-flux component. This new field replaces *NUPDRAFTS*, which was a two-dimensional integer field showing how many updrafts (or plumes) are active at that timestep. Since the number of plumes has now been fixed to eight, with the size of the maximum plume varying according to the criteria in section 4.1, the plume sizes can be represented in a more continuous manner compared to previous scheme versions, where the maximum width was directly related to the number of plumes.

7.5 Height of the Highest-Rising Plume (ZTOP_PLUME)

ZTOP_PLUME is a two-dimensional field which shows the height of the highest-reaching plume in meters at each horizontal location. This always corresponds to the largest plume active within a grid column, since the entrainment rate is inversely proportional to the plume diameter. Note that this is a new field that replaces the old field *KTOP_SHALLOW*, which was shared with the Grell-Freitas shallow-cumulus scheme. As a reminder, all stand-alone shallow-cumulus schemes should be deactivated when configured to run with the MYNN-EDMF's mass-flux component (*bl_mynn_edmf* = 1), otherwise there can be a double-counting of nonlocal mixing processes and cloud representation. Furthermore, duplicate representation of processes can negatively impact the performance of each individual component and complicate the understanding of model behavior as well as efforts to improve model performance.

8. Code Description

8.1 The MYNN-EDMF Submodule

Dr. Mikio Nakanishi freely offered the original version of the MYNN PBL scheme code. Mariusz Pagowski then transformed this code into Fortran 90 with WRF-specific code compliance. Joseph Olson and coauthors then introduced many subsequent modifications, additional features, and eventually removed the WRF-specific code compliance to universalize the scheme for general use in multiple modeling frameworks. Moving to a universalized MYNN-EDMF scheme is an important step in centralizing the scheme development, but creating a publicly accessible stand-alone submodule repository is also necessary to make the code connectable to any modeling framework in which it may be used. Together, this effort has facilitated the ease of developing and testing the same code with colleagues working on different projects, using different models, while studying distinct boundary-layer regimes at different spatial scales.

The current location of the universalized MYNN-EDMF submodule is: https://github.com/NCAR/MYNN-EDMF.git. Within this submodule, the universalized scheme *module_bl_mynnedmf.F90* is located in the top-level directory. The model-specific drivers (each with the same name *module_bl_mynnedmf_driver.F90*) are located in their respective subdirectories named after each model framework that the submodule is currently connected to (WRF, MPAS, and CCPP). The drivers handle the translation of arrays and variables to required input form (i.e., transform model arrays [3D or 2D] to scheme arrays [1D] and the conversion of units between model and scheme). There are also model-specific "common" modules (each with the same name *module_bl_mynnedmf_common.F90*) located in their respective model-framework subdirectories which are used to gather host-specific physical constants and may also hold certain scheme parameters for facilitating tuning for specific dynamical cores.

8.2 Description of subroutines

In most model frameworks, the boundary-layer schemes are called after the radiation, surface-layer, and land-surface models. These three schemes collectively calculate the necessary surface and radiative forcing required for input to the boundary-layer schemes: u_*, *HFX*, *QFX*, *z/L*, and *RTHRATEN* (radiation temperature tendency). After the boundary-layer scheme is called, the gravity-wave/orographic drag, urban, and wind farm parameterization schemes are called, followed by the convection scheme and the microphysics scheme. After the calls to all of the physics schemes, the horizontal diffusion, advection, and filters are applied at the end of the timestep.

Within the MYNN-EDMF, there is a dependency check for the first timestep. If true, several arrays are initialized and *k*-oriented (vertical) subroutines are called at every horizontal point. We describe the function of these subroutines below:

- **GET_PBLH**: Calculates the hybrid θ_v-u_* (or θ_v-*TKE*) PBL height.
- **SCALE_AWARE**: Calculates the similarity functions, $P_{\sigma\text{-}PBL}$ and $P_{\sigma\text{-}shcu}$, to control the scale-adaptive behavior for the local and nonlocal components, respectively.

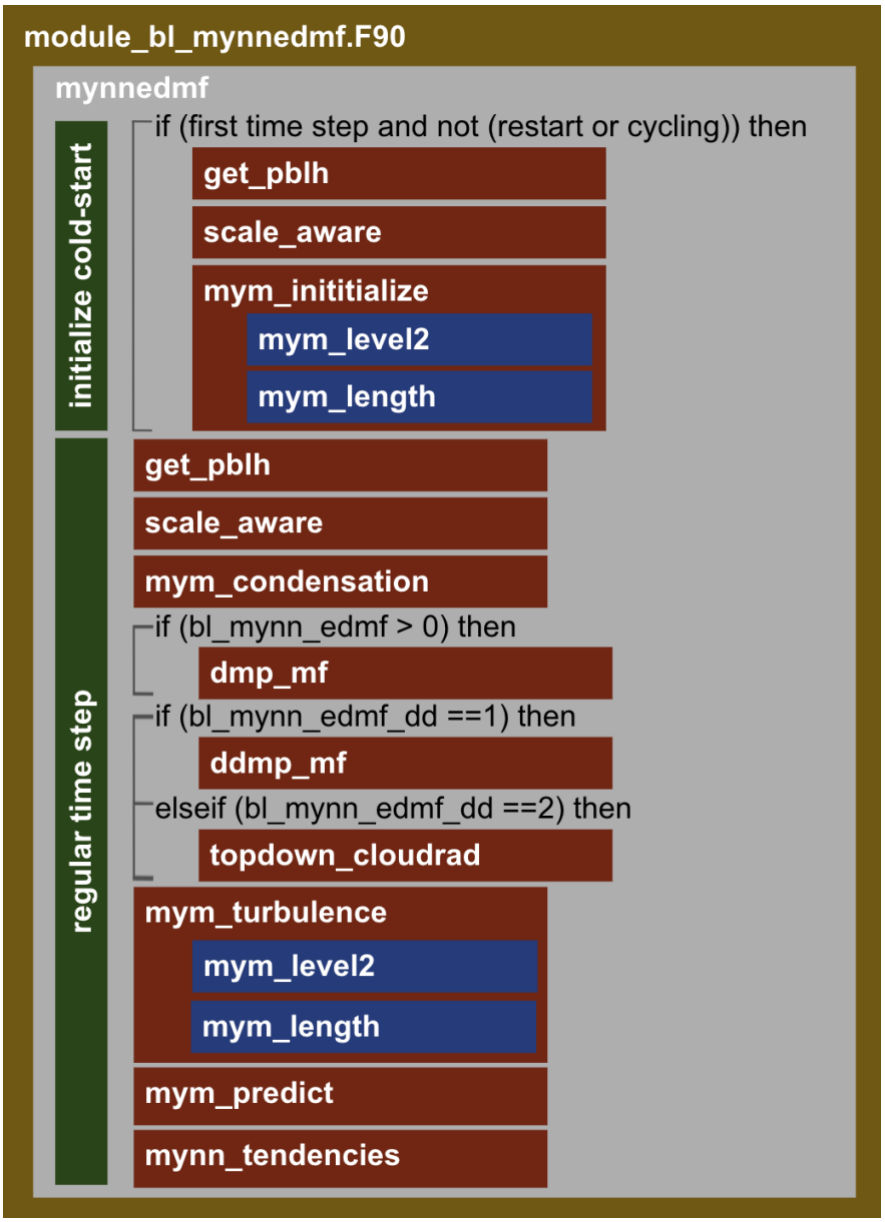

Figure 7. The order of subroutines within the MYNN-EDMF module file, represented by the gold-brown. The main subroutine mynnedmf, represented by gray, organizes the sequence of subroutine calls. The red rectangles are the primary subroutines and the blue rectangles are subroutines called within the primary subroutines. Some tertiary subroutines containing various calculations are not shown.

- **MYM_INITIALIZE**: initializes the mixing length, TKE, θ'^2, q'^2, and $\theta' q'$. These variables are calculated after obtaining prerequisite variables by calling the following subroutines from within **MYM_INITIALIZE**:
    - **MYM_LEVEL2**: Calculates the effective static stability determined by the namelist option *bl_mynn_ess*, non-dimensional wind shear G_M and vertical temperature gradient G_H as well as the level-2 stability functions S_H and S_M.
    - **MYM_LENGTH**: calculates the mixing lengths.

After initializing all required variables, the regular procedures performed at every timestep are ready for execution. The main subroutine **MYNNEDMF** encompasses the primary set of subroutines that contain all procedures that ultimately solve for tendencies of U, V, θ, q_v, q_c, and q_i. The order of primary subroutines called within **MYNNEDMF** is shown in Fig. 7.

Descriptions to the set of procedures is given below:

- **GET_PBLH**: Calculates the hybrid θ_v-u_* (or θ_v-*TKE*) PBL height diagnostic.
- **SCALE_AWARE**: Calculates the similarity functions, $P_{\sigma\text{-}PBL}$ and $P_{\sigma\text{-}shcu}$, which control the scale-adaptive behavior for the local and nonlocal components, respectively.
- There is some important interstitial code after **SCALE_AWARE** that computes the buoyancy flux (or virtual temperature flux) *fltv*, which is used to recompute the reciprocal of the Obukhov length ($1/L$) using the updated surface scalar fluxes and u_* input to the MYNN-EDMF scheme. The surface stability parameter z/L is then used to compute the stability functions used for the lower-boundary condition of TKE as well as the surface-layer length scale.
- **MYM_CONDENSATION**: Calculates the nonconvective (or stratus) component of the subgrid cloud fraction and mixing ratios as well as the buoyancy-flux functions, which are used to calculate the effective static stability (when *bl_mynn_ess* = 0). Different cloud PDFs can be selected by use of the namelist parameter *bl_mynn_cloudpdf*, as described in section 5.1.
- **DMP_MF**: Calculates the nonlocal turbulent transport from the dynamic multi-plume mass-flux scheme as well as the shallow-cumulus (or convective) component of the subgrid clouds. Note that this mass-flux scheme is called when the namelist parameter *bl_mynn_edmf* is set to 1 (recommended). The convective updrafts provide a buoyancy production of TKE, which is added to the TKE budget. If *bl_mynn_edmf* is set to 2, an explicit method is used for solving the nonlocal tendencies from the mass-flux component. By default (*bl_mynn_edmf* = 1), an implicit method is used. The explicit option may be removed, pending further investigation, since there is typically very little difference.
- **DDMP_MF**: Calculates the nonlocal turbulent transport using the 5-plume downdraft model, when the namelist parameter *bl_mynn_edmf_dd* = 1. This method calculates a buoyancy production of TKE from the downdrafts, which is added to the TKE budget. This downdraft model uses an implicit solution when *bl_mynn_edmf* = 1 but is solved explicitly when *bl_mynn_edmf* = 2.
- **TOPDOWN_CLOUDRAD**: Calculates the nonlocal diffusion using the analytical profile method. This method also calculates a buoyancy production of TKE from cloud-top cooling, which is added to the TKE budget. This is only activated when the namelist parameter *bl_mynn_edmf_dd* = 2 (set to 0 by default). This option is likely to be removed in future versions.
- **MYM_TURBULENCE**: First, two subroutines are called within this subroutine to collect the necessary variables to carry out successive calculations:
    - **MYM_LEVEL2**: Calculates the effective static stability determined by the namelist option *bl_mynn_ess*, the nondimensional wind shear G_M and vertical temperature gradient G_H, as well as the level 2 stability functions S_H and S_M, which are subcomponents of all higher-order stability functions.
    - **MYM_LENGTH**: calculates the mixing lengths.
    - Then stability criteria from Helfand and Labraga (1989) are applied.

    - The stability functions for level 2.5 (also used for levels 2.6 and 2.7) or level 3.0 are calculated.
    - If level 3.0 is used, nonzero counter-gradient terms are calculated.
    - Production terms of TKE, θ'^2, q'^2, and $\theta' q'$ are calculated.
    - Eddy diffusivity K_H and eddy viscosity K_M are calculated. For level 2.7, the total turbulent energy (TTE) is added to the TKE prior to calculating K_M.
    - TKE budget terms are calculated (if the namelist parameter *tke_budget* is set to 1).
- **MYM_PREDICT**: solves the prognostic equations for TKE and, if running at higher levels, may also solve for q'^2 (level 2.6+), θ'^2 (level 2.7+), and $\theta' q'$ (level 3.0). If configured to run at a closure level below 3.0, some of the high-order moments will be diagnosed, making them less accurate. In this case, some constraints are added to limit pathological behavior.
- After the TKE is updated, the heating due to dissipation of TKE is calculated if the hard-coded parameter *dheat_opt* (located near the beginning of *module_bl_mynnedmf.F90*) is set to 1. This is set to 1 by default.
- **MYNN_TENDENCIES**: solve for tendencies of U, V, θ, q_v, q_c, and q_i. Depending on the setting for *bl_mynn_mixaerosols*, the aerorsols (*qnwfa*, *qnifa*, and *qnbca*) may be mixed, and depending on the setting for *bl_mynn_mixnumcon*, the number concentrations (*qnc* and *qni*) may also be mixed. All of these variables are checked to make sure they are present. If not present, they are not mixed regardless of the namelist settings. Note that the subgrid-scale clouds are not prognosed; they are only diagnosed and used to complement the resolved-scale clouds prognosed by the microphysics scheme.

8.3 Summary of MYNN-EDMF Namelist Options

Table 4. Description of the namelist options controlling the configurations of the MYNN-EDMF.

Namelist Option	Value	Description and Default Configuration
bl_mynn_mixlength	0	Original form from Nakanishi and Niino (2009)
	1	HRRR operational form 201609–201807. Designed to work without the mass-flux scheme.
	2	HRRR operational form 201807–present. Designed to be compatible with mass-flux scheme activated. (default)
bl_mynn_cloudpdf	0	Use Sommeria-Deardorff subgrid cloud PDF, uses higher-order moments
	1	Use Kuwano-Yoshida subgrid cloud PDF, uses first-order derivatives
	2	Use heavily modified Chaboureau-Bechtold subgrid cloud PDF (default)
bl_mynn_edmf	0	Deactivate mass-flux scheme
	1	Activate dynamic multi-plume mass-flux scheme with implicit solver (default)
	2	Activate dynamic multi-plume mass-flux scheme but use explicit solver
bl_mynn_edmf_mom	0	Deactivate momentum transport in mass-flux scheme (default)
	1	Activate momentum transport in dynamic multi-plume mass-flux scheme. bl_mynn_edmf must be set to 1.
bl_mynn_edmf_tke	0	Deactivate TKE transport in mass-flux scheme (default)
	1	Activate TKE transport in dynamic multi-plume mass-flux scheme. bl_mynn_edmf must be set to 1.
bl_mynn_cloudmix	0	Deactivate the mixing of any water species mixing ratios
	1	Activate the mixing of all water species mixing ratios (default)
bl_mynn_mixqt	0	Mix individual water species separately (default)
	1	Mix total water, then back out individual species. DO NOT USE
bl_mynn_ess	0	Use buoy-flux functions to calculate effective static stability
	1	Use modified O'Gorman (2011) to calculate effective static stability (default)
bl_mynn_tkeadvect	F	Deactivate TKE advection (default)
	T	Activate TKE advection
bl_mynn_mixaerosols	0	Deactivate the mixing of qnwfa, qnifa, and qnbca (when present)
	1	Activate the mixing of qnwfa, qnifa, and qnbca (when present). (default)
bl_mynn_mixnumcon	0	Deactivate the mixing of qnc and qni (when present) (default)
	1	Activate the turbulent mixing of qnc and qni (when present).
bl_mynn_mixscalars	0	Deactivate the generic 4D scalar array (default)
	1	Activate the turbulent mixing all species added to the generic 4D scalar array.
icloud_bl	0	Deactivate coupling of subgrid clouds to radiation
	1	Activate subgrid cloud coupling to radiation (default; highly suggested)

9. Summary, Notes, and Future Work

Over the years, the development of the MYNN-EDMF has been primarily in the context of the RAP/HRRR physics suite. The primary challenges have always been the precise quantification of the model errors and the uncertainty associated with error attribution. Interactions between the parameterized turbulent mixing and other model components, such as radiation, land-surface processes, convection, and microphysics can cause feedbacks that lead to ambiguity in assessing the true source of errors. Changes made to any of these other components may also lead to behavioral changes in the MYNN-EDMF, which will then need to be requantified. Much of the development has happened in a diverse hierarchical framework, exploring model behavior in 3D-cycled, 3D cold-start (global or regional), as well as single-column model (SCM) reported by Angevine et al. (2018). Observations have been critical to the evaluation of the scheme in different locations and geophysical variables (Turner et al. 2020). Over a decade of experience in physics suite-based modeling has helped to more confidently distinguish the errors attributable to the MYNN-EDMF and alleviate biases found in a wide variety of weather and climate regimes spanning from the tropics to the poles.

The fundamental reason why novel boundary layer schemes often perform poorly in practical (real weather) applications is likely because they are not adequately tuned to work well with the rest of the suite of physical parameterizations and/or may be particularly susceptible to unphysical input state variables and/or fluxes that are computed in other components of the land-ocean-atmospheric model. It takes extensive testing to uncover the weaknesses in a scheme and properly address them, whether through a thorough redesign to simpler implementations of well-chosen limits. The simpler end of this spectrum has been recently coined *minor-looking treatments* by Kawai et al. (2022), and we acknowledge their importance in physical parameterization scheme development. When required, we try to set liberal limits that preserve the full range of the observed phase space of a given physical quantity (on Earth). Some quantities may seem needlessly bounded, but when using methods like Stochastic Parameter Perturbations (SPP), which is already implemented in the MYNN-EDMF (Kalina et al. 2021) for enhancing ensemble spread, some additional bounding becomes necessary. We have tried to be transparent about some important tuning/thresholding that can at least partially govern the behavior of the MYNN-EDMF.

There are many new features and options presented in this memorandum. Not all of them are well tested but have been added because we consider them to be mature enough to be made available for testing by the wider community. We realize the growing number of configuration options can seem complicated. We have chosen to keep some internal (hard-coded) options within the scheme to avoid further complication. We have also tried to include advice on how to properly configure the MYNN-EDMF and what to expect from various configuration options. When in doubt, stay with the default setting, which has undergone the most significant testing and is likely the most robust configuration useful for research and operational forecasting applications.

Further testing and developing of the MYNN-EDMF is planned for the foreseeable lifetime of physics-based modeling, as we think physics modeling will remain important for developing training datasets for artificial intelligence-based models well into the future. All current components of the MYNN-EDMF will undergo continuous development and calibration as we work to further generalize this scheme for all regimes, climates, and applications. We have

included some notes on ongoing and near-future work to current and new components/extensions below:

i. *Further work on turbulence linked to cloud-top cooling*

The newest subroutine in the MYNN-EDMF contains the downdraft component. The size and depth of the observed turbulent features linked to cloud-top cooling suggest a downdraft mass-flux component may be the optimal approach to properly represent these features. A possible extension of this new component to upper-level clouds remains unclear despite the pronounced wispy nature of cirrus clouds, which suggests there is significant turbulent transport that needs to be represented. The impact of this new component appears small at short-range forecasts but is not yet well quantified at mid- or long-range forecasts. We anticipate further adjustments will be needed to other components of the MYNN-EDMF, like the subgrid clouds, before it is proven to fit in well and become part of the default configuration.

ii. *The TTE configuration*

The practical forecast advantages of the TTE configuration are not well known, as most of the new TTE schemes remain in research mode instead of advancing to use in operational forecasting systems. The MYNN-EDMF already had some TTE traits built in, so we did not expect a significant change in behavior, but there are some small but systematic changes, like increased 10-m wind speeds in the polar regions, decreased 10-m wind speeds in the tropics, and slightly thicker cloud cover in stratocumulus regions. This latter change may be more due to the addition of θ'^2 for use in the cloud PDF when running at level 2.7 as opposed to just having q'^2 when running at level 2.6. In any case, there may be some forecast benefit when using this relatively new option, but much more testing is required.

iii. *An MYNN-EDMF-based ensemble*

The many configuration options of the MYNN-EDMF may seem daunting to new users, but they may also usefully serve as a basis for a forecast ensemble. The foundations of a potential ensemble system could include MYNN-EDMF members varying the closure levels (*bl_mynn_closure* = 2.5, 2.6, 2.7, and 3.0), mixing length options (*bl_mynn_mixlength* = 0, 1, and 2), cloud PDF options (*bl_mynn_cloudpdf* = 0, 1, and 2), as well as secondary impact options like the effective static stability option (*bl_mynn_ess* = 0 and 1) and the mixing of number concentrations (*bl_mynn_mixnumcon* = 0 and 1). When combining these options with the stochastic parameter perturbations (Kalina et al. 2021) and possibly other stochastic methods such as tendency perturbations, this hypothetical ensemble may provide adequate spread while maintaining reasonable ensemble skill reliability. We are currently in planning stages of applying a configuration-based phase space to a prototype ensemble system.

iv. *Further work on prognostic subgrid-scale (SGS) clouds*

The diagnostic cloud PDF schemes currently in the MYNN-EDMF assume that the PDF variance responds to changes in the higher-order moments or subgrid-scale convective transport. However, in reality, the sources of the PDF variance can be linked to other processes, such as aerosols,

precipitation, and/or interactions between cloud species. A more physically suitable method may be to replace the diagnostic relationship with a prognostic approach. Examples of PDF-based prognostic schemes include Tompkins (2002) or the PC2 scheme of Wilson et al. (2008). Some prognostic schemes that incorporate subgrid-scale vertical motion have also been developed (Lappen and Randall 2001). With prognostic higher-order moments already available in the MYNN-EDMF when run at higher closure levels, an extension to a prognostic SGS cloud approach may be a computationally feasible next step. We have begun testing a new prognostic cloud extension of the TEMPO microphysics scheme that couples to the MYNN-EDMF SGS clouds to explore this path.

v. *Extension to 3D turbulence*

Most of the development of the MYNN-EDMF has been at scales outside or in the upper extent of the boundary layer grey zone where the 1D approximation of turbulence can produce a realistic representation for operational applications. However, there is mounting evidence that a more complete 3D representation of turbulence can further improve simulations in the upper portion of the boundary-layer grey zone (Boutle et al. 2014; Kosović et al. 2020; Zhu et al. 2025) and it has been clear for decades that it is absolutely necessary at finer grid spacing. We intend to extend the MYNN-EDMF so it can be applied seamlessly at any model grid spacing, allowing us to explore the primary impacts of horizontal turbulent fluxes on the growth of the boundary layer, the organization of shallow cumulus, flows in complex terrain, and tropical cyclones.

Acknowledgments: The authors would like to thank Dr. Mikio Nakanishi for sharing the original version of the MYNN PBL scheme and offering helpful insight and advice as the scheme was further developed. Funding for this work was provided by many sources, collectively helping to develop a variety of components of the MYNN-EDMF scheme. These agencies/programs include NOAA's Atmospheric Science for Renewable Energy (ASRE) program, the Federal Aviation Administration (FAA), NOAA's UFS-R2O project, and the U.S. DOE Office of Energy Efficiency and Renewable Energy. The views expressed are those of the authors and do not necessarily represent the official policy or position of any funding agency. We are grateful to the NSF National Center for Atmospheric Research Mesoscale and Microscale Meteorology Laboratory, which has been helpful in integrating and maintaining the MYNN-EDMF in their atmospheric models, and specifically grateful for help from Jimy Dudhia, Wei Wang, and Dave Gill. We are also grateful for help from the Common Community Physics Package (CCPP) code managers, specifically Grant Firl, Dustin Swales, and Dom Heinzeller. We would like to thank Dr. John Brown for years of insightful conversations on modeling, weather, and turbulence.

References

Abdella, K. and N. McFarlane, 1997: A new second-order turbulence closure scheme for the planetary boundary layer. *J. Atmos. Sci.,* **54,** 1850–1867.

Ahmadov, R., and Coauthors, 2017: Using VIIRS fire radiative power data to simulate biomass burning emissions, plume rise and smoke transport in a real-time air quality modeling system. *IEEE International Geoscience and Remote Sensing Symposium (IGARSS)*, Fort Worth, TX, USA, 2017, pp. 2806-2808, doi:10.1109/IGARSS.2017.8127581.

Angevine, W.M., H. Jiang, and T. Mauritsen, 2010: Performance of an eddy diffusivity–mass flux scheme for shallow cumulus boundary layers. *Mon. Wea. Rev.,* **138**, 2895–2912, doi:10.1175/2010MWR3142.1

Angevine, W. M., J. B. Olson, J. S. Kenyon, W. Gustafson, S. Endo, K. Sušelj, 2018: Shallow cumulus in a mesoscale model evaluated with the LASSO framework. *Mon. Wea. Rev*., **146**, 4303-4322, doi:10.1175/MWR-D-18-0115.1

Angevine, W. M., J. B. Olson, J. S. Gristey, I. Glenn, G. Feingold, and D. D. Turner, 2020: Scale awareness, resolved circulations, and practical limits in the MYNN–EDMF boundary layer and shallow cumulus scheme. *Mon. Wea. Rev.*, **148**(11), 4629-4639, doi:10.1175/MWR-D-20-0066.1

Benjamin, S. G., and Coauthors, 2016: A North American hourly assimilation and model forecast cycle: the Rapid Refresh. *Mon. Wea. Rev.,* **144**, 1669–1694, doi:10.1175/MWR-D-15-0242.1

Benner, T. C., and J. A. Curry, 1998: Characteristics of small tropical cumulus clouds and their impact on the environment. *J. Geophys. Res.*, **103**, 28,753–28,767.

Bernardet, L., and Coauthors, 2024: Common Community Physics Package: Fostering collaborative development in physical parameterizations and suites. *Bull. Amer. Meteor. Soc*., **105**, E1490-E1505, doi:10.1175/BAMS-D-23-0227.1.

Blackadar, A. K., 1962: The vertical distribution of wind and turbulent exchange in a neutral atmosphere. *J. Geophys. Res.*, **67**, 3095-3102, doi:10.1029/JZ067i008p03095

Bougeault, P. and P. Lacarrere, 1989: Parameterization of orography-induced turbulence in a mesobeta-scale model. *Mon. Wea. Rev*., **117**, 1872–1890, doi:10.1175/1520-0493(1989)117,1872:POOITI.2.0.CO;2.

Boutle, I. A., Eyre, J. E. J., and Lock, A. P., 2014: Seamless stratocumulus simulation across the turbulent gray zone. *Mon. Wea. Rev*. **142**, 1655–1668.

Brast, M., R. A. J. Neggers, and T. Heus, 2016: What determines the fate of rising parcels in a heterogeneous environment? *J. Adv. Model. Earth Syst.*, **8**, 1674–1690, doi:10.1002/2016MS000750.

Bretherton, C. S., J. R. McCaa, and H. Grenier, 2004: A new parameterization for shallow cumulus convection and its application to marine subtropical cloud-topped boundary layers. Part I: Description and 1D results. *Mon. Wea. Rev.,* **132**, 864–882, doi:10.1175/1520-0493(2004)132<0864:ANPFSC>2.0.CO;2

Brient, F., F. Couvreux, N. Villefranque, C. Rio, and R. Honnert, 2019: Object-oriented identification of coherent structures in large eddy simulations: Importance of downdrafts in stratocumulus. *Geophys. Res. Lett.* **46**, 2854–2864. doi:10.1029/2018GL081499

Canuto, V. M., Y. Cheng, A. M. Howard, and I. N. Easu, 2008: Stably stratified flows: A model with no Ri(cr). *J. Atmos. Sci.*, **65**, 2437–2447, doi:10.1175/2007JAS2470.1.

Chaboureau, J.-P., and P. Bechtold, 2002: A simple cloud parameterization derived from cloud resolving model data: Diagnostic and prognostic applications. *J. Atmos. Sci.*, **59**, 2362–2372, doi:10.1175/1520-0469(2002)059<2362:ASCPDF>2.0.CO;2.

Chaboureau, J.-P., and P. Bechtold, 2005: Statistical representation of clouds in a regional model and the impact on the diurnal cycle of convection during Tropical Convection, Cirrus and Nitrogen Oxides (TROCCINOX). *J. Geophys. Res.*, **110**, D17103, doi:10.1029/2004JD005645.

Cheinet, S., 2003: A multiple mass-flux parameterization for the surface-generated convection. Part I: Dry plumes. *J. Atmos. Sci.,* **60**, 2313–2327, doi:10.1175/1520-0469(2003)060<2313:AMMPFT>2.0.CO;2

Chen, X., and G. H. Bryan, 2021: Role of Advection of Parameterized Turbulence Kinetic Energy in Idealized Tropical Cyclone Simulations. *J. Atmos. Sci*., **78**, 3593–3611, doi:10.1175/JAS-D-21-0088.1.

Colbert, M, D. J. Stensrud, P. M. Markowski, and Y. P. Richardson, 2019: Processes associated with convection initiation in the North American Mesoscale Forecast System, Version 3 (NAMv3). *Wea. Forecast*ing, **34**, 683-700, doi:10.1175/WAF-D-18-0175.1

Cuxart, J., P. Bougeault, and J.-L. Redelsperger, 2000: A turbulence scheme allowing for mesoscale and large-eddy simulations. *Q. J.R. Meteorol. Soc*., **126**: 1-30.

Cuxart, J., A and Coauthors, 2006: Single-column model intercomparison for a stably stratified atmospheric boundary layer. *Boundary-Layer Meteorol*., **118**, 273–303.

de Roode, S. R., A. P. Siebesma, H. J. Jonker, and Y. de Voogd, 2012: Parameterization of the vertical velocity equation for shallow cumulus clouds. *Mon. Wea. Rev.,* **140**,2424–2436, doi:10.1175/MWR-D-11-00277.1

Deardorff, J. W., 1970: Convective velocity and temperature scales for the unstable planetary boundary layer and for Rayleigh convection. *J. Atmos. Sci.,* **27**, 1211–1213.

Deardorff, J. W., 1980: Cloud-top entrainment instability. *J. Atmos. Sci.*, **37**, 131–147.

Dowell, D. C., and Coauthors, 2022*:* The High-Resolution Rapid Refresh (HRRR): An hourly updating convection-allowing forecast model. Part I: Motivation and system description. *Wea. Forecasting*, **37**, 1371–1395, doi:10.1175/WAF-D-21-0151.1.

Duynkerke, P. G. and Driedonks, A. G. M., 1987: A model for the turbulent structure of the stratocumulus-topped atmospheric boundary layer. *J. Atmos. Sci.* **44**, 43–64.

Duynkerke, P. G., 1991: Radiation fog: a comparison of model simulation with detailed observations, *Mon. Wea. Rev.* **119**, 324–342.

Esau, I. N. and Ø. Byrkjedal, 2007: Application of a large-eddy simulation database to optimisation of first-order closures for neutral and stably stratified boundary layers. *Bound.-Layer Meteorol.,* **125**(2), 207-225. doi:10.1007/s10546-007-9213-6

Fitch, A. C., J. K. Lundquist, and J. B. Olson, 2013: Mesoscale influences of wind farms throughout a diurnal cycle. *Mon. Wea. Rev.*, **141**, 2173–2198, doi:10.1175/MWR-D-12-00185.1.

Furuichi, N., T. Hibiya, and Y. Niwa, 2012: Assessment if turbulence closure models for resonant inertial response in the oceanic mixed layer using a large eddy simulation model. *J. Oceanography.*, **68**, 285-194.

Galperin, B., S. Sukoriansky, and P. S. Anderson, 2007: On the critical Richardson number in stably stratified turbulence. *Atmos. Sci. Lett.*, **8**, 65–69, doi:10.1002/asl.153.

Gambo, K., 1978: Notes on the turbulence closure model for atmospheric boundary layers. *J. Meteor. Soc. Japan*, **56**, 466–480.

Garratt, J. R., 1992: The Atmospheric Boundary Layer. Cambridge University Press, 316 pp.

Golaz, J., V. E. Larson, and W. R. Cotton, 2002: A PDF-based model for boundary layer clouds. Part I: method and model description. *J. Atmos. Sci.,* **59**, 3540–3551, doi:10.1175/1520-0469(2002)059<3540:APBMFB>2.0.CO;2

Grenier, H., and C. S. Bretherton, 2001: A moist PBL parameterization for large-scale models and its application to subtropical cloud-topped marine boundary layers. *Mon. Wea. Rev*, **129,** 357–377.

Ha, K.-J. and L. Mahrt, 2001: Simple inclusion of z-less turbulence within and above the modeled nocturnal boundary layer. *Mon. Wea. Rev.,* **129**(8), 2136-2143.

Han, J. and C. S. Bretherton, 2019: Scale-aware TKE-based moist eddy-diffusivity mass-flux (EDMF) parameterization for vertical turbulent mixing interacting with cumulus convection. *Wea. Forecasting*, **34**, 869-886, doi:10.1175/WAF-D-18-0146.1

Harris, L., X. Chen, W. Putman, L. Zhou, and J.-H. Chen, 2021: A Scientific Description of the GFDL Finite-Volume Cubed-Sphere Dynamical Core. 109 pp., doi:10.25923/6nhs-5897.

Helfand, H. M. and J. C. Labraga, 1988: Design of a nonsingular level 2.5 Second-order closure model for the prediction of atmospheric turbulence. *J. Atmos. Sci.,* **45**, 113–132, doi:10.1175/1520-0469(1988)045<0113:DOANLS>2.0.CO;2.

Hobbs, P. V., 1974: High concentrations of ice particles in a layer cloud. *Nature*, **251,** 694–696, doi:10.1038/251694b0

Honnert R., V. Masson, and F. Couvreux, 2011: A diagnostic for evaluating the representation of turbulence in atmospheric models at the kilometric scale. *J. Atmos. Sci*., **68**, 3112–3131.

Ito, J., H. Niino, M. Nakanishi, and C.-H. Moeng, 2015: An extension of the Mellor–Yamada model to the terra incognita zone for dry convective mixed layers in the free convection regime. *Boundary-Layer Meteorol*, **157**, 23-43. doi:10.1007/s10546-015-0045-5

James, E. P., and Coauthors, 2022*:* The High-Resolution Rapid Refresh (HRRR): An hourly updating convection-allowing forecast model. Part II: Forecast performance. *Wea. Forecasting*, **37**, 1397–1417, doi:10.1175/WAF-D-21-0130.1.

Janjić, Z., 2002: Nonsingular implementation of the Mellor–Yamada level 2.5 scheme in the NCEP meso model. NCEP Office Note No. 437, pp. 60

Jankov, I., and Coauthors, 2017: A performance comparison between multiphysics and stochastic approaches within a North American RAP ensemble. *Mon. Wea. Rev*., **145**, 1161–1179, doi:10.1175/MWR-D-16-0160.1.

——, J. Beck, J. Wolff, M. Harrold, J. B. Olson, T. Smirnova, C. Alexander, and J. Berner, 2019: Stochastically perturbed parameterizations in an HRRR-based ensemble. *Mon. Wea. Rev*., **147**, 153–173, doi:10.1175/MWR-D-18-0092.1.

Kalina, E. A., I. Jankov, T. Alcott, J. Olson, J. Beck, J. Berner, D. Dowell, and C. Alexander, 2021*:* A progress report on the development of the high-resolution Rapid Refresh ensemble. *Wea. Forecasting*, **36**, 791–804, doi:10.1175/WAF-D-20-0098.1.

Katata, G., H. Nagai, T. Wrzesinsky, O. Klemm, W. Eugster, and R. Burkard, 2008: Development of a land surface model including cloud water deposition on vegetation. *J. Appl. Meteor. Climatol.,* **47**, 2129–2146, doi:10.1175/2008JAMC1758.1

Kawai, H., K. Yoshida, T. Koshiro, and S. Yukimoto, 2022: Importance of minor-looking treatments in global climate models. *J. Adv. Model. Earth Sys.*, **14**, e2022MS003128, doi:10.1029/2022MS003128

Kim. J. and L. Mahrt, 1992: Simple formulation of turbulent mixing in the stable free atmosphere and nocturnal boundary layer. *Tellus*, **44A**, 381-394.

Kitamura, Y., 2010: Modifications to the Mellor-Yamada-Nakanishi-Niino (MYNN) model for the stable stratification case. *J. Meteor. Soc. Japan*, **88**, 857–864, doi:10.2151/ jmsj.2010-506.

Köhler, M., M. Ahlgrimm, and A. Beljaars, 2011: Unified treatment of dry convective and stratocumulus-topped boundary layers in the ECMWF model. *Q. J. R. Meteorol. Soc.*, **137**, 43-57.

Koracin, D., and R. Berkowicz, 1988*:* Nocturnal boundary-layer height: Observations by acoustic sounders and prediction in terms of surface-layer parameters. *Bound.-Layer Meteor.*, **43,** 65–83.

Kosović, B. and J. A. Curry, 2000: A large eddy simulation study of a quasi-steady, stably stratified atmospheric boundary layer. *J. Atmos. Sci.*, **57**, 1052–1068, doi:10.1175/ 1520-0469(2000)057,1052:ALESSO.2.0.CO;2.

Kosović, B., Munoz, P. J., Juliano, T. W., Martilli, A., Eghdami, M., Barros, A. P., and Haupt, S. E., 2020: Three-dimensional planetary boundary layer parameterization for high-resolution mesoscale simulations. *J. of Physics: Conference Series.* **1452**, 1-10.

Kurowski, M.J. and J. Teixeira, 2018: A scale-adaptive turbulent kinetic energy closure for the dry convective boundary layer. *J. Atmos. Sci.,* **75**, 675–690, doi:10.1175/JAS-D-16-0296.1

Kuwano-Yoshida, A., Enomoto, T. and Ohfuchi, W., 2010: An improved PDF cloud scheme for climate simulations. *Q.J.R. Meteorol. Soc*., **136**: 1583-1597. doi:10.1002/qj.660

Lauritzen, P. H., Kevlahan, N. K.-R.,Toniazzo, T., Eldred, C., Dubos, T.,Gassmann, A., et al., 2022: Reconciling and improving formulations for thermodynamics and conservation principles in Earth System Models (ESMs). *Journal of Advances in Modeling Earth Systems*, **14,** e2022MS003117. doi:10.1029/2022MS003117

Lemone, M. A. and W. T. Pennell, 1976: The relationship of trade wind cumulus distribution to subcloud layer fluxes and structure. *Mon. Wea. Rev.,* **104**, 524–539, doi:10.1175/1520-0493(1976)104<0524:TROTWC>2.0.CO;2

Lemone, M. A., M. Tewari, F. Chen, and J. Dudhia, 2013: Objectively determined fair-weather CBL depths in the ARW-WRF model and their comparison to CASES-97 observations. *Mon. Wea. Rev.*, **141**, 30–54, doi:10.1175/MWR-D-12-00106.1.

Lemone, M. A., M. Tewari, F. Chen, and J. Dudhia, 2014: Objectively determined fairweather NBL features in ARW-WRF and their comparison to CASES-97 observations. *Mon. Wea. Rev*., **142**, 2709–2732, doi:10.1175/MWR-D-13-00358.1.

Lenderink, G. and A. A. M. Holtslag, 2004: An updated length-scale formulation for turbulent mixing in clear and cloudy boundary layers. *Q. J. R. Meteorol. Soc*., **130**, 3405–3427. doi:10.1256/qj.03.117

Lenderink G. and A. A. M. Holtslag, 2000: Evaluation of the kinetic energy approach for modeling turbulent fluxes in stratocumulus. *Mon. Wea. Rev.,* **128**, 244–258.

Li, H., Ahmadov, R., J. Romero-Alvarez, G. A. Grell, J. B. Olson, J. Schnell, and Coauthors, 2025: Enhancing aerosol direct feedback for numerical weather prediction in NOAA's rapid refresh forecast system–smoke and dust (RRFS-SD v1). *Geophysical Research Letters*, **52**, e2025GL115384. doi:10.1029/2025GL115384

Lock, A. and J. Mailhot, 2006: Combining non-local scalings with a TKE closure for mixing in boundary layer clouds. *Boundary-Layer Meteorol.* **121**, 313–338.

Machulskaya, E. and D. Mironov, 2020: The stability functions and realizability of the turbulent kinetic energy–scalar variance closure for moist atmospheric boundary-layer turbulence. *Bound.-Layer Meteor*. **176**(2), 197-228, doi:10.1007/s10546-020-00528-7

Mahrt, L. and D. Vickers, 2003: Formulation of turbulent fluxes in the stable boundary layer. *J. Atmos. Sci.,* **60**, 2538–2548, doi:10.1175/1520-0469(2003)060<2538:FOTFIT>2.0.CO;2

Mauritsen, T., G. Svensson, S. S. Zilitinkevich, I. Esau, L. Enger, and B. Grisogono, 2007: A total turbulent energy closure model for neutrally and stably stratified atmospheric boundary layers. *J. Atmos. Sci.*, **64,** 4113–4126.

Mellor, G. L., 1977: The Gaussian cloud model relations. *J. Atmos. Sci*, **34**, 356-358.

Mellor, G. L. and T. Yamada, 1974: A hierarchy of turbulence closure models for planetary boundary layers. *J. Atmos. Sci.*, **31**, 1791–1806, doi:10.1175/1520-0469(1974)031,1791: AHOTCM.2.0.CO;2.

Mellor, G. L. and T. Yamada, 1982: Development of a turbulence closure model for geophysical fluid problems. *Rev. Geophys. Space Phys.*, **20**, 851–875, doi:10.1029/RG020i004p00851.

Mishra, S., D. L. Mitchell, D. D. Turner, and R. P. Lawson, 2014: Parameterization of ice fall speeds in midlatitude cirrus: Results from SPartICus, *J. Geophys. Res. Atmos*., **119**, 3857–3876, doi:10.1002/2013JD020602.

Nakanishi, M., 2000: Large-eddy simulation of radiation fog. *Bound. Layer Meteor.*, **94**, 461-493.

Nakanishi, M., 2001: Improvement of the Mellor–Yamada turbulence closure model based on large-eddy simulation data. *Bound. Layer Meteor.*, **99**, 349–378.

Nakanishi, M. and H. Niino, 2004: An improved Mellor–Yamada level-3 model with condensation physics: Its design and verification. *Bound. Layer Meteor.*, **112**, 1–31.

Nakanishi, M. and H. Niino, 2006: An improved Mellor–Yamada level-3 model: Its numerical stability and application to a regional prediction of advection fog. *Bound. Layer Meteor*., **119**, 397– 407.

Nakanishi, M. and H. Niino, 2009: Development of an improved turbulence closure model for the atmospheric boundary layer. *J. Meteor. Soc. Japan,* **87,** 895–912, doi:10.2151/jmsj.87.895.

Neggers, R.A., H.J. Jonker, and A.P. Siebesma, 2003: Size statistics of cumulus cloud populations in large-eddy simulations. *J. Atmos. Sci.,* **60**, 1060–1074, doi:10.1175/1520-0469(2003)60<1060:SSOCCP>2.0.CO;2

Neggers, R. A. J., M. Köhler, and A. Beljaars, 2009: A dual mass flux framework for boundary layer convection. Part I: Transport. *J. Atmos. Sci.*, **66**, 1465–1487.

Neggers, R. A. J., 2015: Exploring bin-macrophysics models for moist convective transport and clouds. *J. Adv. Model. Earth Syst.*, **7**, 2079–2104, doi:10.1002/2015MS000502.

Nichols S. and J. D. Turton, 1986: An observational study of the structure of stratiform cloud sheets: Part II. Entrainment. *Q. J. R. Meteorol. Soc.*, **112** (472), 461-480.

Nielsen-Gammon, J. W. and Coauthors, 2008: Multisensor estimation of mixing heights over a coastal city. *J. Appl. Meteor. Climatol.*, **47**, 27–43, doi:10.1175/2007JAMC1503.1.

Nieuwstadt, F. T. M., 1984: The turbulent structure of the stable, nocturnal boundary layer. *J. Atmos. Sci*., **41**, 2202-2216.

Olson, J. B., T. Smirnova, J. S. Kenyon, D. Turner, J. M. Brown, W. Zheng, and B. W. Green, 2021: A description of the MYNN Surface-Layer Scheme. NOAA Tech. Memo. OAR GSL-67, 26 pp., doi:10.25923/f6a8-bc75.

Olson, J. B., J. S. Kenyon, W. M. Angevine, J. M. Brown, M. Pagowski, and K. Sušelj, 2019a: A description of the MYNN-EDMF scheme and coupling to other components in WRF-ARW. NOAA Tech. Memo. OAR GSD-61, 37 pp., doi:10.25923/n9wm-be49.

Olson, J. B., and Coauthors, 2019b: Improving wind energy forecasting through numerical weather prediction model development. *Bull. Amer. Meteor. Soc*., **100**, 2201-2220, doi:10.1175/BAMS-D-18-0040.1

Olson, J. B., and J. M. Brown, 2009: A comparison of two Mellor–Yamada-based PBL schemes in simulating a hybrid barrier jet. Preprints, *23rd Conf. on Weather Analysis and Forecasting/19th Conf. on Numerical Weather Prediction,* Omaha, NE, Amer. Meteor. Soc., JP1.13. [Available online at http://ams.confex.com/ams/pdfpapers/154321.pdf.]

Puhales, F. S., J. B. Olson, J. Dudhia, D. Lima de Bem, R. Maroneze, O. Costa Acevedo, F. Denardin Costa, and V. Anabor, 2020: Turbulent kinetic energy budget for MYNN-EDMF PBL scheme in WRF model. Universidade Federal de Santa Maria Technical Note. 9 pp. https://repositorio.ufsm.br/handle/1/28327.

Shin, H. H. and S. Hong, 2013: Analysis of resolved and parameterized vertical transports in convective boundary layers at gray-zone resolutions. *J. Atmos. Sci.,* **70**, 3248–3261, doi:10.1175/JAS-D-12-0290.1

Siebesma, A. P. and J. W. M. Cuijpers, 1995: Evaluation of parametric assumptions for shallow cumulus convection. *J. Atmos. Sci.*, **52**, 650–666.

Siebesma, A. P., and Coauthors, 2003: A large-eddy simulation intercomparison study of shallow cumulus convection. *J. Atmos. Sci.*, **60**, 1201–1219.

Siebesma, A. P., P. M. M. Soares, and J. Teixeira, 2007: A combined eddy-diffusivity mass-flux approach for the convective boundary layer, *J. Atmos. Sci.*, **64**, 1230–1248.

Simpson, J. and V. Wiggert, 1969: Models of precipitating cumulus towers, *Mon. Weather Rev.*, **97**, 471–489.

Skamarock, W. C. and Coauthors, 2019: A description of the Advanced Research WRF version 4. NCAR Tech. Note NCAR/TN-556+STR, 162 pp. [Available online at http://www2.mmm.ucar.edu/wrf/users/docs/technote/v4_technote.pdf]

Skamarock, W. C., J. B. Klemp, M. G. Duda, L. D. Fowler, S. Park, and T. D. Ringler, 2012: A Multiscale Nonhydrostatic Atmospheric Model Using Centroidal Voronoi Tesselations and C-Grid Staggering. *Mon. Wea. Rev*., **140**, 3090–3105, doi:10.1175/MWR-D-11-00215.1.

Soares, P. M. M., P. M. A. Miranda, A. P. Siebesma, and J. Teixeira, 2004: An eddy-diffusivity/mass-flux parameterization for dry and shallow cumulus convection. *Quart. J. Roy. Meteor. Soc.*, **130**, 3365–3384.

Sommeria, G. and J. W. Deardorff, 1977: Subgrid-scale condensation in models of nonprecipitating clouds. *J. Atmos. Sci.*, **34**, 344–355, doi:10.1175/1520-0469(1977)034,0344:SSCIMO.2.0.CO;2.

Sorbjan, Z., 1991: Evaluation of local similarity functions in the convective boundary layer. *J. Appl. Meteor.*, **30,** 1565–1583.

Steeneveld, G. J., B. J. H. van de Wiel, and A. A. M. Holtslag, 2007: Diagnostic equations for the stable boundary layer height: Evaluation and dimensional analysis. *J. Appl. Meteor. Climatol*., **46**, 212-225, doi:10.1175/JAM2454.1.

Stull, R. B., 1988: An Introduction to Boundary Layer Meteorology. Kluwer Academic, 666 pp.

Sun, J., 2011: Vertical variations of mixing lengths under neutral and stable conditions during CASES-99. *J. Appl. Meteor. Climatol.,* **50**, 2030–2041, doi:10.1175/JAMC-D-10-05006.1

Sušelj, K., T. F. Hogan, and J. Teixeira, 2014: Implementation of a stochastic eddy-diffusivity/mass-flux parameterization into the Navy Global Environmental Model. *Weather and Forecasting*, **29**, 1374–1390, doi:10.1175/WAF-D-14-00043.1.

Teixeira, J. and S. Cheinet, 2004: A simple mixing length formulation for the eddy-diffusivity parameterization of dry convection. *Bound. Layer. Meteorology*, **110**: 435–453. doi:10.1023/B:BOUN.0000007230.96303.0d

Teixeira, J. and A. P. Siebesma, 2000: A mass-flux/K-diffusion approach for the parametrization of the convective boundary layer: global model results. Pp. 231– 234 in Proceedings of 14th Symposium on Boundary Layers and Turbulence, (Aspen, Co), American Meteorol. Soc., Boston, USA.

Tian, Y. and Z. Kuang, 2016: Dependence of entrainment in shallow cumulus convection on vertical velocity and distance to cloud edge. *Geophys. Res. Letters*, **43** (8), 4056–4065. doi:10.1002/2016gl069005.

Tompkins, A. M., 2002: A prognostic parameterization for the subgrid-scale variability of water vapor and clouds in large-scale models and its use to diagnose cloud cover. *J. Atmos. Sci.* **59**, 1917–1942.

——, 2008: Cloud Parameterization. In *Proceedings of Workshop on Parametrization of sub-grid physical processes*. ECMWF, Reading, U.K. Available at https://www.ecmwf.int/sites/default/files/elibrary/2009/12778-cloud-parametrization.pdf

Turner, D.D., J. Hamilton, W. Moninger, M. Smith, B. Strong, R. Pierce, V. Hagerty, K. Holub, and S.G. Benjamin, 2020: A verification approach used in developing the Rapid Refresh and other numerical weather prediction models. *J. Oper. Meteor*., **8**, 39-53, doi:10.15191/nwajom.2020.0803

Turner, D. D., M. D. Shupe, and A. B. Zwink, 2018: Characteristic atmospheric radiative heating rate profiles in Arctic clouds as observed at Barrow, Alaska. *J. Appl. Meteor. Climatol*., **57**, 953–968, doi:10.1175/JAMC-D-17-0252.1.

Wadler, J. B., D. S. Nolan, J. A. Zhang, L. K. Shay, J. B. Olson, and J. J. Cione, 2023: The effect of advection on the three-dimensional distribution of turbulent kinetic energy and its generation in idealized tropical cyclone simulations. *J. Adv. Model. Earth Sys.*, **15**, e2022MS003230. doi:10.1029/2022MS003230

Wilson, D. R., A. C. Bushell, A. M. Kerr-Munslow, J. D. Price and C. J. Morcrette, 2008: PC2: A prognostic cloud fraction and condensation scheme. I: Scheme description. *Q. J. R. Meteorol. Soc.*, **134**, 2093–2107. doi:10.1002/qj.333

Wilson, T. H. and R. G. Fovell, 2018: Modeling the evolution and life cycle of radiative cold pools and fog. *Weather and Forecasting*. **33**, 203–220, doi:10.1175/WAF-D-17-0109.1

Witek, M.L., J. Teixeira, and G. Matheou, 2011: An integrated TKE-based eddy diffusivity/mass flux boundary layer closure for the dry convective boundary layer. *J. Atmos. Sci.,* **68**, 1526–1540, doi:10.1175/2011JAS3548.1

Wyngaard, J., O. Coté, and Y. Izumi, 1971: Local free convection, similarity, and the budgets of shear stress and heat flux. *J. Atmos. Sci.*, **28**, 1171–1182.

Xu, K. and D.A. Randall, 1996: A Semiempirical cloudiness parameterization for use in climate models. *J. Atmos. Sci.,* **53**, 3084–3102, doi:10.1175/1520-0469(1996)053<3084:ASCPFU>2.0.CO;2

Yuan, T., 2011: Cloud macroscopic organization: Order emerging from randomness. *Atmos. Chem. Phys.*, **11**(15), 7483–7490, doi:10.5194/acp-11-7483-2011.

Zhu, P. and Coauthors, 2025: Toward a unified parameterization of three dimensional turbulent transport in high resolution numerical weather prediction models. *npj Climate and Atmospheric Science*, **8**:**223**, 1-13, doi:10.1038/s41612-025-01117-6

Zilitinkevich, S. S., T. Elperin, N. Kleeorin, and I. Rogachevskii, 2007: Energy- and flux-budget (EFB) turbulence closure model for stably stratified flows. Part I: Steady-state, homogeneous regimes. *Bound.-Layer Meteor*., **125**, 167–191, doi:10.1007/s10546-007-9189-2.